Understanding helium diffusion in iron: a multiscale modelling method based on the DFT and kinetic Monte Carlo, coupled to TEM and thermo-desorption spectroscopy experiments

Vinicius Oliveira Cavalcanti, Jérôme Roques, Aurélie Gentils, Denis Horlait, Eric Gilabert, Laurent Tassan-Got

Understanding helium diffusion in iron: a multiscale modelling method based on the DFT and kinetic Monte Carlo, coupled to TEM and thermo-desorption spectroscopy experiments

Vinicius Oliveira Cavalcanti[1], Jérôme Roques[1*], Aurélie Gentils[1], Denis Horlait[2], Eric Gilabert[2], Laurent Tassan-Got[1]

[1] Université Paris-Saclay, CNRS/IN2P3, IJCLab, 91405, Orsay, France

[2] Université de Bordeaux, CNRS, LP2i Bordeaux, UMR5797, Gradignan, France

* Corresponding author: jerome.roques@ijclab.in2p3.fr

Accepted in Journal of Nuclear Materials
Journal of Nuclear Materials 583 (2023) 154511

https://doi.org/10.1016/j.jnucmat.2023.154511

Abstract

Helium (He) is known to accumulate in vacancies of the steel structure materials of nuclear reactors, forming bubbles that increase in size and eventually cause structural problems, such as embrittlement. Several studies provided insights into the interstitial diffusion of this gas inside the iron matrix. However, much is still unknown about its behaviour. Based on this context, this study proposes a new combined theoretical and experimental multiscale approach made by the same team in a complementary way. It helps to have a global view of the helium diffusion in iron as a function of He content, temperature and structural defect concentration.

Firstly, density functional theory has been used to identify the possible helium insertion sites in iron and the possible transitions between them. Then, the kinetic Monte Carlo method was applied to calculate its interstitial diffusion coefficient. It showed that helium swiftly diffuses interstitially in iron. It also tends to be trapped in iron vacancies and accumulate. The chromium and vacancy effects were also investigated.

Experimentally, He was ion-implanted in several pure iron and high-purity Fe10wt%Cr samples. An analysis of He behaviour and its diffusion was carried out with transmission electron microscopy (TEM) and thermo-desorption spectroscopy (TDS) techniques. TEM shows the presence of small (~0.7 nm radius) He bubbles and no significant difference with the presence of Cr. TDS evidences sequential “burst-type” He releases as T is sequentially increased. Based on these observations and inferred from the literature, we propose that He is detrapped and released from the studied materials as a consequence of the decrease in maximum He capacity of the trapping aggregates as T increases.

1. Introduction

Ferritic steels are possible candidates for future nuclear reactors due to their resistance to high pressure, temperature and irradiation conditions[1,2]. However, helium accumulation inside steels remains a severe problem for nuclear materials. Firstly, it is known that He is not soluble in metals[1,3,4]. It is also mobile in steel and tends to be trapped in vacancies, then accumulate and form bubbles[5–9]. These are responsible for structural damage with swelling and embrittlement at high temperatures[3,10–16]. This phenomenon could pose a significant problem in future nuclear reactors, especially for the proposed fusion reactors. They produce helium due to the transmutation reactions, such as (n,α) and direct α-production[1,3,17,18]. The ratio of He concentration (in appm) and displacements per atom (dpa) in future fusion reactor materials is expected to be around 10 to 20 appm He/dpa[19,20]. These conditions will be harsh to be withstood by the materials involved with the blanket and wall barriers of the reactors. Using circa 9 wt.%Cr may improve the materials to withstand these conditions better. They have already been used in the reduced activation ferritic/martensitic (RAFM) steels, such as CLAM and Eurofer97, and show a low ductile-brittle transition temperature (DBTT) and a smaller hardening gain caused by the irradiation[18,21–24].

Based on this problem, it is fundamental to understand more about He diffusion inside steels and the bubbles formation mechanisms to improve the material's resistance against them. The density functional theory (DFT) has been a valuable tool for modelling helium behaviour at an atomic scale and obtaining helium formation and binding energies to vacancy clusters[3,25]. The He insertion sites in iron were already identified, and their energies were calculated based on DFT[26–28]. Some possible migrations between these sites were observed, and their migration energies were evaluated by the use of the drag[27] and Nudged elastic band (NEB)[29] methods. Nevertheless, the diffusion coefficient calculations based on these energy results are lacking. This work proposes a combined approach (DFT/ kinetic Monte Carlo) to achieve this outcome.

The effect of chromium (Cr) in lowering the swelling in the materials and changing the He diffusion was also observed. For example, the insertion of Cr changed the helium insertion energy and the migration energy value, which was studied using the NEB method[29,30]. The vacancies' effects were also studied, such as the vacancy formation energy and its impact on the helium insertion energy[5,29,31]. The accumulation of He inside a monovacancy and the formation of He_nV_m (following the Kroger-Vink notation[32])clusters were studied, where V represents the vacancies, n is the quantity of He atoms, and m is the number of vacancies[1,3,17,18,33]. However, much is still uncertain about this system: the migration mechanism is still not wholly understood; the diffusion coefficient of helium in iron is not well characterised, and neither is the influence of Cr and vacancies on it. In addition, the accumulation of helium inside a monovacancy is a controversial topic with mixed results[1,3,17,33]. Therefore, a complete study of helium diffusion is still necessary to better understand He behaviour in Fe (and Fe(Cr)) and the consequences to the materials subjected to it.

Experimentally, the diffusion and behaviour of helium have also been studied to some extent. Ono et al. studied the He bubbles behaviour using transmission electron microscopy (TEM) in pure Fe and Fe-9wt%Cr alloys[34]. He ions with 10 keV energy were implanted under a fluence of 5×10^{13} $He.cm^{-2}$ at temperatures between 200 and 800 ºC. The motion of the bubbles and their size distribution at 400 and 600 ºC were then described. It seemed that Cr slows the diffusivity of the bubbles. Later, they also investigated the thermo-desorption spectroscopy (TDS) spectra of both materials implanted with 5 keV He at 85 and 473 K with the fluences of $1\text{-}2\times10^{16}$ He/cm^2. The results show a shift to higher temperatures for the release of He in the case of Cr, probably due to chromium precipitation around the bubbles, visualised by STEM-EELS[35]. Sugano et al. investigated the effect of different Cr concentrations on the helium diffusion with both TDS and TEM after implanting 8 keV He ions at room temperature with fluences from 2×10^{13} to 2×10^{15} $He.cm^{-2}$. They proposed a He-V migration mechanism, which is disturbed by the presence of Cr[36]. Xu et al. demonstrated that He desorption in pure iron occurs at two moments: mainly at higher temperatures (from 880 ºC) and at the α-γ

transition[37]. However, they could not have a clear TDS signal at low fluences of 1×10^{11} and 1×10^{13} He.cm^{-2}. Yu et al. studied the implantation of helium ions at 100 keV with a fluence of 6×10^{16} He.cm^{-2} in pure iron films with TEM and showed their low He bubble density compared to bulk iron and the attraction of the bubbles to grain and phase boundaries[38]. Lefaix et al. studied, using TDS, the helium desorption from pure iron implanted samples at 8 keV and 3 MeV with a fluence of 1-2×10^{16} He.cm^{-2}. They showed that impurities (0.5% carbon in their case) might significantly affect the release of He at higher temperatures and that the helium diffusion is probably through the progressive de-trapping of helium bubbles[39]. Zhu et al. studied the effect of the dislocations and other defects in Fe9Cr implanted at room temperature with 0.2 keV and 3 keV under a fluence of 4.2×10^{14} and 4.2×10^{15} He.cm^{-2} using TDS. They showed that vacancies and dislocations delay the He diffusion by capturing He atoms and that the alpha-gamma transition releases a high amount of trapped atoms around 865 ^{o}C[40].

From this literature review, one can observe that there is a lack of results that analyse and compare the helium bubbles behaviour at both Fe and Fe10Cr materials at low and high fluences in the same experimental conditions. A model of helium diffusion based on TDS results is also lacking. In addition, studies that combine experimental and theoretical results are rare. There is a need for a comprehensive study of iron and iron-chromium alloys using both methods, which motivates this work.

This article tries to understand and characterise the He diffusion in Fe with a multi-approach not used before for this system. It is based on calculations at an atomic and macroscopic scale completed with TDS and TEM. Firstly, a bulk iron model is optimised and validated using DFT. Second, the possible helium insertion sites are identified, and their insertion energies are calculated. Then, the pathways between these He positions are determined by the nudged elastic band (NEB) method and the transition state theory (TST). Finally, the kinetic Monte Carlo (KMC) algorithm simulates the He atom's trajectory as a function of the temperature and allows it to express its diffusion

coefficient. The influence of iron vacancies and chromium substitution on the diffusion coefficient is also considered. Experimentally, "pure" iron and high purity Fe10%wtCr samples were implanted with helium ion and characterised using transmission electron microscopy (TEM) and thermo-desorption spectroscopy (TDS) techniques from low to higher helium fluences.

2. Materials and methods

2.1. Theoretical part

The calculations required for the iron structure optimisation and the investigation of the possible insertion sites were performed with the method of periodic density functional theory (DFT)[41] implemented in the VASP (Vienna ab-initio simulation program) code [42,43]. A plane-wave basis set is used for the total energy calculations, and the project augmented plane wave (PAW) method is applied to describe the valence electron interactions and the representation of the core electrons[44,45]. Three functionals were employed: the local density approximation (LDA) and the generalised gradient approximation (GGA), the Perdew-Burke-Ernzerhof (PBE) and the Perdew-Wang (PW91)[46–48]. Eight ($3d^7 4s^1$), twelve ($3p^6 4s^1 3d^5$), and two electrons ($1s^2$) are considered valence ones for Fe, Cr, and He, respectively. The calculation parameters were optimised, and the value used for the cut-off energy is 400 eV with Gaussian smearing of 0.2 eV. The basis cubic iron cell (2 atoms) is not large enough to avoid the relaxation of the structure when a He is inserted. Therefore, an optimised supercell of 4×4×4 is created (with 128 atoms). The Monkhorst-Pack scheme[49] was employed to sample the Brillouin zone (BZ), and the optimised *k*-point mesh of 17×17×17 was used for the unit cell and 4×4×4 for the supercell. These parameters were adopted to guarantee an energy convergence of 10^{-6} eV per atom until the Hellmann-Feynman forces are less than 10^{-5} eV/Å. All calculations were performed with spin-polarisation treatment.

After optimising the iron supercell, the helium insertion sites were characterised by their formation energies. Then, the nudged elastic band (NEB) method[50] was used to calculate the migration energy between each stable insertion site and to identify the minimum energy path (MEP) between them. [51,52]. The spring constant value used in our calculations was 5 eV/Å^2. The saddle point was identified and then optimised using the climbing image NEB (CI-NEB) for a more accurate description[53]. This interstitial diffusion mechanism is based on the random trajectory of the He atoms inside the iron structure. It is a thermally activated process and can be correctly described by the transition state theory (TST)[54–58] and by the Vineyard approximation[55]. More methodology details are present in our previous works[59–62].

These values are calculated once the transition state is correctly identified, and the jump probability will be an input value for KMC simulations[63,64]. The advantage is the possibility of extending the simulations' time scale to model the diffusion of an atom based on a stochastic approach with the jump probabilities and energies.

Moreover, combining the KMC and the TST principles is necessary to address the case of a heterogeneous crystal with Cr-substitutions or vacancies. The sum of the reciprocal of the jump probabilities is equal to the time required to pass from one interstitial site to another, called residence time. The diffusion coefficient at a determined temperature (D_T) can be calculated based on an Einstein equation, relating the time and the mean square displacement (D). It is used for helium diffusion[61,65–67]. It is mathematically defined in (Eq.1).

$$D_T = \frac{<r^2(t)>}{2 \times d \times t} \qquad \text{(Eq.1)}$$

Where $< r^2(t) >$ is the mean square displacement; d is the diffusion dimension (in this case, three as all the directions inside the crystal are considered); t is the time.

Using this expression, the diffusion coefficient can be calculated for different temperatures. Based on these values, the Arrhenius equation[68] is used to obtain a general relation between the diffusion coefficient and the temperature, as expressed in (Eq.2).

$$D_T = D_0\, e^{-\frac{E_a}{k_B T}} \qquad \text{(Eq.2)}$$

Where D_0 is a pre-exponential factor; and E_a is the effective activation energy. Both D_0 and E_a can then be calculated from a linear regression of a ln D_T versus $\frac{1}{k_B T}$ plot.

2.2. Experimental part

The experimental part involves the preparation of pure iron and high-purity Fe10Cr samples, $^4He^+$ ions implantations, and the post-characterisation by Transmission Electron Microscopy (TEM) and Thermo-Desorption Spectroscopy (TDS).

2.2.1. Materials and ion implantation

The pure iron sample is a Goodfellow ultrapure (99.99%) square material, while the chromium material is a high-purity bulk Fe10Cr (10.54 at.% Cr, or 9.86 wt.%) cylindrical material with approximately 1 cm in diameter specially fabricated by the École Nationale Supérieure des Mines, Saint-Etienne, France. After chemical etching with nitral, an optical microscope was used to measure the grains size in the samples, which are in the order of several micrometres. The samples were prepared before ion implantation: firstly, they were cut into squares of 5x5x0.5 mm. They were then mechanically polished using conventional silicon carbide abrasive paper with diamond polishing solutions with multiple grain sizes down to 0.5 μm to remove surface damages.

The ion implantations were performed at the JANNuS-Orsay MOSAIC platform of IJCLab (Orsay, France) [69,70]. The 190 kV ion implanter IRMA equipped with a Bernas-Nier source was employed. The fluences of 1×10^{13}, 1×10^{14}, 1×10^{15} and 1×10^{16} He ion/cm^2 were selected. The Stopping and Range of Ions in Matter (SRIM-2008) code [71] was applied to visualise the implanted He ions' profile and choose the implantation energy of 50 keV based on the depth of the samples. The calculations considered full damage cascades displacement energy of 40 eV for iron, considering a previous result from the literature [72]. The resulting distribution profile of He ions as a function of the depth predicted by SRIM is visible in Figure 1. The implantations were performed at room temperature, and the mean ion flux was the same for all implantations, equal to 1×10^{12} cm^{-2}s^{-1}. The following fluences were used: 1×10^{13} cm^{-2}, 1×10^{14} cm^{-2}, 1×10^{15} cm^{-2}, 1×10^{16} cm^{-2}. The damage and damage rate values calculated for the maximum fluence 1×10^{16} cm^{-2}, based on the SRIM results, are 0.56 dpa and 5.6 $\times10^{-5}$ dpa/s. The damage profile for the highest fluence is visible in Figure 1. The peak maximum (circa 200 nm) corresponds to a He concentration close to 0.8 at.%. The implantations were done under vacuum and with the samples positioned orthogonally to the incident He ion beam.

2.2.2. Transmission electron microscopy (TEM)

After helium ion implantation, the samples were studied by two different techniques. The first is conventional TEM at the JANNuS-SCALP platform[69,70] using a 200 kV FEI Tecnai G^2 20 Twin microscope with LaB_6 filament and equipped with a Gatan imaging filter (GIF) tridiem apparatus, used here for thickness measurements using Electron Energy Loss Spectroscopy (EELS) as detailed in [73]. Cross-section TEM thin foils were extracted by the Focused Ion Beam standard lift-out technique at IEMN, Lille; their thicknesses were measured by EELS for each studied zone and were in the range of 40-75 nm. The conventional cavity imaging technique using through-focal series was employed to visualise the presence of any cavities or helium bubbles in both samples as a function of

the helium ion implantation depth: cavities appear white surrounded by a dark fringe in underfocused conditions and black surrounded by a white fringe in overfocused conditions (not shown here).

2.2.3. Thermo-desorption spectroscopy (TDS)

The second experimental technique is thermo-desorption spectroscopy (TDS). The samples were transported to the LP2i Bordeaux, where the PIAGARA platform (French acronym for Interdisciplinary Platform for Noble Gas Analysis) is used to detect rare gases down to ultra-trace levels by using mass spectrometry (MS)[74,75]. Thus, it allows precise measurements of helium release from the specimens as a function of the temperature and time. The setup employed for the present study is described in [75], with an experimental approach close to ref. [74], and both can be consulted for more details. Briefly, the installation consists of 4 different parts: 1) a heating chamber setup from where the gas is extracted by heating the sample with a continuous wave laser; 2) the separation and purification system to trap all released gases but He; 3) a ^{3}He spike calibration system and 4) a mass spectrometer (MS) for the analysis (A Micromass 12 from VG modified to be able to perform rare gases measurements)[74]. In addition to these components, several pumps are employed to guarantee the ultra-high vacuum conditions required by these experiments (routinely 10^{-12} bar)[74].

The laser heating beam, whose power profile is changed from its natural Gaussian shape to a top-hat shape, illuminates the sample and its support (a degassed stainless-steel sheet) with a circa 15-20 mm diameter to ensure sample temperature homogeneity while limiting the chamber heating. Real-time measurement and control of the sample temperature are done using different pyrometers. For the present study covering an extended temperature range, three complementary pyrometers were used: an Optris Csmicro (8 – 14 µm; -50 to 1030 °C; spot size Ø of ~11 mm), a Raytek MM2MHVF1L (1.6 µm; 450 to 2250 °C; spot size Ø <1 mm) and a Sensortherm Metis M322 (1.45 – 1.65 µm; 600 to 2300 °C; spot size Ø of ~0.8 mm). A PID system controls the laser power source to adjust the temperature and produce any desired temperature plateau or ramp with less than a 1 °C deviation

between the targeted and measured temperature. For T < 600 °C, the Optris pyrometer was selected as the input data for temperature control, and this was switched to the Sensortherm one for T > 600 °C once the two pyrometers' temperatures were coincided (see after). For metallic materials such as Fe and Fe(Cr), emissivities ε are relatively low. More annoyingly, their ε are strongly temperature, wavelength and surface-finish (rugosity) dependent[76–78], bringing significant uncertainties on the true sample temperature. Several data exist on Fe[79] (and references therein) and Fe(Cr)[79] emissivities, but they are sometimes contradictory and do not fulfil our needs. This phenomenon is particularly true for the lowest temperatures and the Optris pyrometer (8-14 μm). In addition, the impossibility of such a far-IR wavelength to focus optically leads to a measurement area more significant than the sample size. Fortunately, it was experimentally found that little or no He was released below 450°C, the temperature for which the Raytek pyrometer would start given experimental values. For the Raytek and Sensortherm pyrometers, data from J. Taylor [76] accounted for the monotonous ε increase with T. According to Touloukian and DeWitt[79] for the Raytek and Sensortherm pyrometer, the emissivity setup is regularly increased. Also, fortunately, Fe and Fe(Cr) display their α to γ phase transition variations of sample visual aspect and “accidents” in the temperature and power ramp signals. This transition was used to correct all measured temperatures (e.g. if a pyrometer found the expected 912 °C phase transition occurring at 930 °C, its formerly measured data was *a posteriori* corrected by a 912/930 correction ratio). The temperature error is estimated to evolve from virtually 0 °C at the temperature of phase transition to ±20°C at the start (~450 °C) and end (~1200 °C) of He release.

During the experiments, the heating chamber was directly connected to the spectrometer through a purification zone. The released He gas was treated by purification devices to trap all gases but He (and Ne) in flight. Before starting the sample heating, an aliquot of a reference gas containing precisely known ^{3}He and ^{4}He quantities is let in the working volume. The idea is not directly to measure ^{4}He quantities released by the sample but to deduce it from the ^{4}He/^{3}He increased measured

ratio. This procedure allows to cancel out any deviations from MS sensitivity that may notably arise if a burst release of gas happens, but mostly it avoids having to correct ^{4}He consumption by the MS (wall implantation). It also allows for correcting, if necessary, the notable contaminations of ^{4}He (through MS memory effects or micro-entry of atmospheric ^{4}He notably) since the ^{4}He/^{3}He ratio is monitored before and after the TDS experiment. The MS is set to continuously measure the ^{4}He/^{3}He ratio with a ~60 s loop. The MS and pyrometers are time-synchronised, and after the aforementioned pyrometry corrections are done, the results are displayed as in, e.g. Figure 9a).

Two types of experiments are performed with samples from all materials. The specimens are heated with a ramp of 5 °C/min from room temperature in the first one. Throughout this process, the evolution of the He release is constantly observed. The temperature increase is made until no more gas is relaxed after an extensive temperature range, or unfortunately, as it numerously happened, when the viewport through which the heating laser enters broke (volatilised Fe at T ≳ 1200°C deposits on the viewport and renders it suddenly opaque to the heating laser). The second type of experiment is the so-called temperature plateaux. Based on the observation of the He release pattern in a material at a given fluence, certain temperatures are chosen, where the gas liberated is measured in these temperatures' plateaux for a few tens of minutes. The objective is to extract ^{4}He apparent diffusion kinetics at each discrete temperature and deduce activation energies through Arrhenius plots. The data obtained fits the models presented and discussed in Section 3.2.2.3, and an equation representing this phenomenon is given.

3. Results and discussion

3.1. Theoretical part

3.1.1. Iron unit cell and validation of calculation parameters

Iron belongs to the space group *Im*-3*m* and has a cubic bcc unit cell with two atoms. Similarly, a supercell was proposed that was expanded four times in all directions (4×4×4) with the equivalent of 128 atoms. Different functionals were compared using other theoretical and experimental results available in the literature to validate the model. The GGA PBE functional showed the best compromise based on the literature results.

3.1.2. Investigation of He insertion sites

With the optimised parameters for the iron unit cell developed using GGA PBE functional (see Section 2.1. for details about model choice), the next step was identifying the possible helium insertion sites in the system. The cell was replicated four times in all directions (4×4×4) to accommodate the He atom. This supercell can contain an extra atom without significant cell relaxation. The lattice parameter is 11.32 Å, and the volume increase with the He presence was small enough (around 0.4%) to validate its size. Due to the BCC character of the Fe unit cell, two possible insertion sites are identified: tetrahedral and octahedral ones and they are presented in Figure 2 (a) and (b), respectively. The results for both sites and the comparison with other theoretical results in the literature are available in Table 1. The similarities between them confirm our model.

3.1.3. Interstitial He migration

All possible neighbour sites and transitions were identified from each site through analysis of the structure. Only the directly connected transitions without an intermediate interstitial site were considered. Two probable transitions were identified. Firstly, from an initial tetrahedral site (hereafter called S1), four equidistant neighbouring tetrahedral sites, named S2, were identified at 1.01 Å (Figure 3-e). It constitutes the first transition called S1-S2. From the same S1 site, two possible tetrahedral neighbouring sites, hereafter called S3, are also found at a 1.41 Å distance. In the middle of this transition, there is an octahedral site (I3(O) in Figure 3-d). It constitutes the last transition named S1-S3. The NEB method was used for each transition to identify the migration path, energy,

and transition state for each case. The results are summarised in Figure 3, with the possible paths for a given site shown in Figure 3-e.

The migration energy values are similar to those in the literature[29,80]. Interestingly, in the transition S1-S3, the actual transition state corresponds to the octahedral interstitial position. This indicates that the supposed interstitial site is not an actual one but a transition state (a similar hypothesis was considered for hydrogen in iron[81]). The migration energy values are small, with 0.06 eV for the S1-S2 transition and 0.20 eV for the other (equal to the energy difference between the tetrahedral and octahedral sites). These first simulations show that these transitions, thus He diffusion in Fe, can occur even below ambient temperatures.

3.1.4. Frequency analysis and validation of the transitions

To apply the KMC method, the vibration frequencies of each interstitial and transition site were calculated. Based on the Vineyard theory[55], the attempt frequency for the S1-S2 transition was calculated as $9.49 \times 10^{12,}$ and the jump probability expression for it is:

$$\Gamma_{S1-S2} = \quad 9.49 \times 10^{12} exp\left(-\frac{0.06}{k_B T}\right) \qquad \text{(Eq.3)}$$

The considered He interstitial sites have three real frequencies (zero imaginary frequencies), and the transition states are the ones with only two real frequencies (one imaginary frequency). It is visible that the transition between S1-S2 corresponds to this, but the one from S1 to S3 does not. This transition has an octahedral site in the middle, theoretically corresponding to the transition state. However, two imaginary frequencies are present at this site instead of one. Thus, it cannot be considered an actual interstitial site (zero imaginary frequency) or a transition site (one imaginary frequency). It is the same behaviour pattern identified with the hydrogen diffusion in iron[81]. The same linear diffusion path was found with a rank-2 saddle point (two imaginary frequencies) in the octahedral site; therefore, it is not an actual transition state, and the Vineyard approximation[55]

cannot be used. A recent theoretical article[82] showed that the diffusion coefficient's effect on second-order transition states is limited, especially at low temperatures (below 1000 K). The same was observed experimentally[83]. Hence, due to these aspects, only the S1-S2 transition (Figure 3-a) is considered for the following steps with the KMC.

3.1.5. Kinetic Monte Carlo and diffusion coefficient calculation

A KMC homemade code was used to calculate the 3D He random trajectories at different temperatures, with 200,000 steps for a general overview of the He trajectory. A random walk trajectory in all three directions is visible already at a low temperature. This happens because the migration energy (0.06 eV) is significantly small. It is then possible to conclude that helium in a perfect Fe cell should diffuse interstitially even at low temperatures.

KMC simulations were performed at different temperatures (from 300 to 3000 K), and the diffusion coefficients were calculated for each temperature from the mean square displacements. Based on the Arrhenius law (Eq.2), the logarithm of D_T versus the inverse of the temperature multiplied by the Boltzmann constant was plotted to calculate the pre-exponential factor ($D_{0,i}$) and the effective activation energy (E_a, i) of He interstitial diffusion in Fe. It allows obtaining the interstitial diffusion coefficient (D_i) expression as a function of temperature. The equation with both parameters is in (Eq.4).

$$D_i = 6.5 \times 10^{-4} \mathrm{e}^{-\frac{0.06}{\mathrm{kT}}} cm^2 s^{-1} \quad \text{(Eq.4)}$$

This equation is valid up to the iron phase transition at 912 °C [84]. The values of the activation energy, $E_{a,i}$ = 0.06 eV, and the pre-exponential factor, $D_{0,i}$ = 6.5 × 10^{-4} cm^2. s^{-1} were obtained. This value of $E_{a,i}$ agrees with previous works, but $D_{0,i}$ is slightly different to the ones found by Li et al.[29]: $E_{a,i}$ = 0.059 eV and $D_{0,i}$ = 2.802 × 10^{-4} cm^2. s^{-1}. The activation energy is the same because it

was also calculated in the same way with the NEB method. For the pre-exponential factor the difference could be explained by the different calculation methods. To grasp the order of magnitude of the helium diffusion in pure iron, D_T was calculated at 1000 K around the highest foreseen operating temperature in the future reactors[85]. The value obtained of 3.23×10^{-4} cm^2. s^{-1} indicates that in a perfect (i.e. defect-free) Fe piece, a generated helium would diffuse out within a few seconds.

3.1.6. Chromium's effect (iron substitution)

Firstly, in the pure 128 iron atomic cell, an iron atom was substituted by a chromium one. The helium atom was inserted in the tetrahedral sites around the chromium atom, and its energy was calculated. Here, the distance of the helium atoms to the chromium one significantly affects its insertion energy. Four different cases were considered: He as the first neighbour of Cr (1nn), as the second neighbour (2nn), as the third one (3nn), and as the fourth one (4nn). The results for each case with the distances are presented in Table 2 and compared to other literature results when available.

The He insertion energy related to the degree of proximity to the chromium atom shows that its value is lightly affected by Cr presence with a ~2% increase (less stability), and the Cr influence fades away with the distance. Fe and Cr's similar atomic radius could explain this (1.30 Å for Cr[86] and 1.24 Å for Fe[87]).

As the next step, the possible transitions available for the He atom are analysed following the same methodology as pure iron. They are the same as in the pure iron case. However, the proximity of the He atom to the Cr one can play a role as it can affect the insertion and migration energies. Therefore, the transitions of the He atom up to the fourth neighbour to the Cr atom were analysed, and their energies were calculated using the NEB method as previously done with pure iron. The four transitions and their migration energies are presented in Figure 4 and compared to another work[88].

Our values agree with Martínez and Fu's ones[88], except for the first neighbour case, where we determine higher stability (~ 0.07 eV) for the He atom around Cr. This phenomenon may come

from the different methods used (drag[88] and, in our case, CI-NEB), as well as different pseudopotentials employed and calculation parameters.

Our results show that transition states have higher energies close to the chromium, inducing a blocking effect. However, a KMC simulation shows that the blocked paths are easily bypassed in 3D and that the diffusion coefficient is marginally reduced for a Cr concentration of 10%. Therefore, we did not consider the Cr in our following models to simplify the calculations.

3.1.7. Vacancy effect

The effect of removing an iron atom and creating a vacancy was studied following the same methodology as before. Firstly, a supercell with 127 Fe atoms (removing the iron atom in the centre) was created and optimised. The vacancy migration energy was calculated using the CI-NEB to verify the model's validity. A value of 0.68 eV was obtained, similar to other values in the literature (0.78[89], 0.55[90]). Then another aspect is considered. To remove this iron atom and create the vacancy, some energy is required, which is called vacancy formation energy (E_V^f) and can be calculated by (Eq.5):

$$E_V^f = E_{(N-1)Fe+V} - \frac{N-1}{N} E_{NFe} \qquad \text{(Eq.5)}$$

Where $E_{(N-1)Fe+V}$ is the energy of the cell with only 127 iron atoms due to the vacancy (V) (here N=128 for a perfect cell) and E_{NFe} is the energy of a perfect cell of iron without vacancies. Our calculated value is 2.17 eV, as seen in Table 3.

Then a helium atom is added to the vacancy and optimised. Its insertion energy is calculated as 2.2 eV, comparable to the value of 2.3 eV from Fu and Williaime[25]. It is more common in the literature to see the formation energy of a substitutional atom (E_{sub}^{f}) of He in an iron lattice. This is described by (Eq.6), where E_{NFe+He} is the energy of the cell with helium in a substitutional position, N is the number of iron atoms in the cell (here 127 for a cell with a vacancy), E_{Fe} is the energy per iron atom in a perfect crystal and E_{He} is the energy of an isolated helium atom. The comparison between our and other results can be seen in Table 3.

$$E_{sub}^{f} = E_{NFe+He} - (NE_{Fe} + E_{He}) \quad \text{(Eq.6)}$$

Our values are similar to the other theoretical and experimental results for both E_{V}^{f} and E_{sub}^{f}, which reaffirms the validity of our calculations. These calculations show the higher stability of a He inside a vacancy as the energy requirement is lower than in a tetrahedral site (4.57 eV).

Once the helium atom is inside a vacancy, the calculations show that it is complicated to leave it due to a trapping effect. A complete relaxation calculation of helium in the two nearest tetrahedral sites (1nn at 1.6 Å and 2nn at 2.6 Å) shows that it tends to return to the centre of the vacancy. The only option for the atom to escape the vacancy is to reach the third nearest tetrahedral site (3nn at 3.2 Å). Once it arrives at this distance, the diffusion follows the same paths as in pure iron, with the shortest tetrahedral-tetrahedral transitions of 1 Å.

Furthermore, the possibility of a single helium atom leaving the vacancy is explored. As done before, the NEB method helps obtain the migration path and energy for the transition between the vacancy and the nearest possible tetrahedral site (hereafter called S1) at 3.23 Å, as shown in Figure 5. The He atom returns to the vacancy when it arrives at the first (1nn) and second nearest interstitial sites (2nn). It can only be placed from the third nearest tetrahedral site (3nn) at a considerable distance, which shows the stability of the He atom in the vacancy and the tendency to be efficiently

trapped by it. Another fact confirming this behaviour is the high migration energy of 2.35 eV required for the atom to arrive at the third nearest interstitial site (Figure 5). At the same time, helium can be easily retrapped, returning to the vacancy from this interstitial site, with a migration energy of 0.05 eV. It indicates the trapping of He by a vacancy and confirms its low solubility in iron[4] and accumulation in vacancies[80,91–93].

Due to the considerable migration energy to leave the vacancy, this transition was considered relevant, and the KMC method was applied to calculate the diffusion coefficient in this scenario. The same procedures were used, and the helium transition attempt frequencies were calculated. The obtained jumping probability expression for the transition Vacancy-S1 is $\Gamma_{Vacancy-S1} = 2.51 \times 10^{12} exp\left(-\frac{2.35}{k_B T}\right)$ and the one for the S1-vacancy is $\Gamma_{S1-Vacancy} = 7.33 \times 10^{12} exp\left(-\frac{0.05}{k_B T}\right)$.

With these results, the KMC method can be used. Here, only the mechanism of diffusion discussed before was used, considering only isolated vacancies, without including the helium cluster diffusion. Unlike the previous situation without vacancies, the percentage of vacancies in the simulation cell can play an important role. The diffusion coefficient is calculated as a function of temperature for a vacancies fraction (nv) varying from 0 (i.e. without vacancies) to 4×10^{-2} (Figure 6). The minimal nv = 5×10^{-9} is limited by the calculation method and still represents an iron material with considerable vacancy concentration due to irradiation.

It is visible that even a tiny presence of vacancies (5×10^{-9}) is responsible for significantly reducing diffusion coefficient values. This is explained by the significantly higher value of activation energy (2.36 eV) to leave the vacancy than the one in pure iron (0.06 eV). The vacancies, therefore, are indispensable for the diffusion model. It is essential to notice that this model is a simplification, as it does not consider the vacancies, He-V clusters, dislocations, and grain boundaries diffusion. Another effect that could be considered is the He diffusion of He_nV_m clusters. For instance, Fu and Willaime showed the diffusion of HeV_2 clusters with an effective migration energy of 1.17 eV [94].

Marian and Bulatov studied the comparison of the interstitial and substitutional He after implantation [95]. Nevertheless, our model is the first step toward elucidating helium diffusion behaviour in Fe(Cr).

In a further step, it is pertinent to understand the vacancy attraction behaviour towards helium and how many helium atoms could be accumulated inside it. This is controversial in the literature as many results have been reported, as shown in Table 4. These differences may come from the calculation methods, parameters employed and chosen He initial positions. For our calculations, helium atoms were progressively added to the vacancy in a cell with 127 Fe atoms, and the cell was relaxed in both frozen (Figure 7-I) and relaxed volumes (Figure 7-II). The He distribution and the closest Fe atoms for each scenario can be seen in Figure 7. The image shows that the vacancy can accommodate many He atoms. The He quantity changes from calculations with a frozen volume or with a relaxed one. Figure 7 (I) shows that a single vacancy could accommodate up to 20 He atoms before a strong iron cell restructuration, while up to 17 in (II) for a relaxed volume. This difference arises from the higher constraint of the iron positions in a fixed volume, as the cell cannot expand enough. In both cases, the same happens when a certain number of He atoms inside the vacancy is surpassed: the pressure around it is sufficient to displace a first neighbour Fe atom, creating a new vacancy and a self-interstitial atom (SIA). This phenomenon was already seen in the literature[1,3,17], explaining the nucleation and growth of He bubbles: He accumulates inside a vacancy up to a threshold, and then a SIA and a new vacancy are created, allowing more He atoms. The process repeats itself, and the bubble grows.

In order to further investigate the stability of He atoms inside a single vacancy, ab-initio molecular dynamics simulations (as implemented in VASP) [42,44] were applied to analyse the temperature's relevance. In these simulations, a constant volume was used to show the effect of constrained atoms and the Brillouin Zone was reduced to one k-point (representing the Γ point) for long-time simulations (steps of 1 fs). This approximation was tested and proved possible as a low

difference of roughly 4% is found between the calculations with one k-point and more. They were run in the NVT canonical ensemble with the Nose-Hoover thermostat[96,97] at different temperatures (300, 500, 800 and 1000 K), and the other convergence parameters from the previous calculations were used. The results showed that many configurations visible in Figure 7 are unstable with temperature, and a SIA is formed quickly. For instance, less than 10 He atoms are stable at 800 K (from 10 atoms, a SIA is created after only 10 ps). In contrast, less than 16 He are stable at 300 K. Hence, the temperature has an essential role as a significantly lower number of He atoms, in comparison to the static-DFT calculations, should be permanently stable in a monovacancy with higher temperatures, approaching some of the results reported in the literature[1,17].

This first theoretical step confirms the tendency of He accumulation in iron vacancies due to its high interstitial diffusion coefficient, allowing it to reach vacancies and then be trapped inside them efficiently. Vacancies have a significant role in helium diffusion behaviour and effective diffusion kinetics at the macroscopic scale, as they are powerful trapping sources. Furthermore, the lastly presented T-dependant simulations and few reference data gathered in Table 4 hint that vacancies may trap fewer and fewer He atoms as T increases, as the present TDS results thereafter will confirm.

3.2. Experimental Part

3.2.1. Transmission electron microscopy (TEM)

Underfocus bright-field (BF) TEM images on thin foils extracted from both Fe and Fe10Cr samples implanted with He ions at a fluence of 1×10^{16} at room temperature are shown in Figure 8. It is noticeable that the cavities, appearing white surrounded by a dark fringe in the underfocus condition, are not perfectly spherical, and their size is close to the resolution limit of the microscope (which has a spatial resolution of 0.27 nm). The cavities' patterns are similar for both Fe and Fe10Cr

samples: they are randomly distributed with a high density across the specimen following the implantation depth profile visible in Figure 1. As these cavities appear after the He ion implantation step, we make here the assumption that they are filled with helium, and thus we call them bubbles in the following.

The bubbles' diameters were obtained, and their distribution inside the material regarding the distance to the surface correlates to the projected range/SRIM profile shown in Figure 1. With a statistic of over 3000 bubbles per sample, the average radius size of the bubbles observed in Fe is 0.7 ±0.2 nm and in Fe10Cr is 0.7 ±0.3 nm with the volumetric density from 0.00059-0.00342 nm^{-3} and from 0.00050-0.00100 nm^{-3} for FeCr. These values are similar to Yu et al.'s, who reported an average value of 0.55 nm in pure iron at room temperature under a fluence of 6×10^{16} He/cm^2 at 100 keV[38]. Henry et al. also reported an average bubble radius of less than 1 nm in a Fe-9Cr-1Mo sample implanted with 34 MeV He ions at 250 ºC, with an implanted concentration close to 0.25 at.%[98]. These results corroborate the bubble formation mechanism that we previously described using DFT. We expect that the bubbles visualised using TEM are formed due to the accumulation of He atoms inside an irradiation-generated defect that grows in size, possibly even with SIAs formation, as more helium accumulates. Our DFT calculations showed a spherical bubble due to He presence up to the formation of the first SIA. Then, it loses the spheric shape with its growth. Our simulated monovacancy cavity diameter is 0.65 nm (i.e. cavity containing one vacancy with the maximum He amount before creating a new SIA), smaller than the average 1.4 nm bubbles visualised by TEM. We expect that these are formed by capturing additional He atoms and emitting SIAs. Furthermore, we saw no significant differences between pure iron and Fe10Cr, similar to our observed theoretical model results, showing that such amount of chromium, implanted at room temperature, did not play a noticeable role in the observed bubbles' features (size and density). It is essential to notice that an implantation fluence lower than 1×10^{16} at/cm^{-2} may also produce He bubbles. However, as we are already within the resolution limit of the microscope, we did not risk investigating them.

3.2.2. Thermo-desorption spectroscopy (TDS)

3.2.2.1. Pure iron samples

At the end of TDS, one sample of each fluence was melted with the He implanted fluences determined by mass spectrometry: 1.10×10^{13}, 0.86×10^{14}, 0.88×10^{15} and 0.57×10^{16} at. cm^{-2} with an associated error of ±5%. Their values were considered in the data treatment, but they are displayed from the initially targeted fluences as a simplification. There was a considerable difference in the higher fluence targeted and obtained values (-43%) probably due to one or several of the following factors: most likely, it is due to a saturation of He in the material, possibly stemming from blistering with the accumulation of implantation damages and saturation of the sample[39,99], corroborated by some defects seen by TEM (dislocations); uncertainties on the flux measurement (the fluence rate of the ion beam has a 1% uncertainty [100]) could have played a minor role; similarly, TDS determination of the fluence could have been at its lower bound; a last but not least possible factor is that Rutherford backscattering may become significantly higher with the increase of the fluence.

In this study, the heating ramp was 5 °C/min from room temperature up to around 1300 °C. The helium release profile for each fluence versus the temperature in the pure iron samples can be seen in Figure 9-ab. Unlike other results, we did not observe a peak before 300 °C [1,2,7]. This peak corresponds to the release of helium from vacancies near the surface. In our case, the higher He implantation energy (50 keV) causes more profound defects in the specimens; hence, the helium is not released by this particular surface-related mechanism.

Three peak regions are identified, with the values varying from each fluence: region I from circa 500-800 °C, region II around 900 °C and III from 1000 to 1200 °C. Region II consists of a sharp peak in Figure 9-b, present in all the fluences. The phase transition temperature of iron ($\alpha \rightarrow \gamma$) is at 912 °C[84], and based on other results[101,102] as well as a sudden concomitant drift of PID, this He burst release is attributed to $\alpha \rightarrow \gamma$ transition, and we used the peak to adjust emissivities and

pyrometry results (as detailed in the Methodology section). Such burst release at the α → γ transition is commonly reported in similar experiments[101,102]. For Peak II, Sugano et al.[101] had explained this sharp peak due to the lower stability of He-vacancy clusters in fcc iron. However, a similar behaviour was also observed by cooling, with a γ → α transition [37]. Ono et al.[35] consider that this release is due to the instability caused by a phase transition around the helium bubbles responsible for the release, a hypothesis also adopted by Xu and Wirth[102]. Considering that the α → γ (or γ → α) transition is exothermic, we hypothesize that the transient increase of T by the phase transition could also participate in this sudden He release, at least on its amplitude [103].

The higher fluences delay the first helium release peak (onset T from ~480 °C for 1.10×10^{13} at.cm^{-2} vs ~640 °C for 1.10×10^{16} at.cm^{-2}). This phenomenon could be related to different mechanisms between higher (from 1×10^{15}) and lower fluences. For 1×10^{13} at. cm^{-2}, the release starts at around 480 °C, with a considerable and fast release up to 540 °C. Then, slow and lower desorption is present between 540 and 750 °C. For 1×10^{14} at. cm^{-2}, it is slightly shifted towards 490 °C, and the desorption is smaller and slower, seemingly combining two pics into one, which also finishes towards 750 °C. In the case of 1×10^{15}, the release is significant from 650 °C, while for 1×10^{16}, it is only from 700 °C with a steep peak (half of He budget released within ~50°C). There is negligible (~3-4% of He budget) desorption for the higher fluences below 600 °C compared to the lower ones. This behaviour could be explained by a change in He desorption mechanism related to the fluence. For instance, a higher fluence is responsible for producing more vacancies and forming more He_nV_m clusters with lower values for n, which are more stable and require more energy to be released (helium binding energy from 1.8 to 5.3 eV[104] in the vacancy-clusters instead of 2.26 eV in a dislocation[105] and 0.4 eV in grain boundaries[106]). Dislocations might be comparatively more present and influential at lower fluences due to the lower matrix damage. According to the model approximating the activation energy of He dissociation from traps as a function of T (see Appendix), the binding energy to the dislocations (2.26 eV [89,99]) matches the onset temperatures of the first

release peaks for 1×10^{13} and 1×10^{14} samples, corroborating this idea. The matrix is damaged with a higher fluence, and the vacancy clusters significantly reduce the possibility of He diffusing out by the dislocation diffusion mechanism without encountering a vacancy trap on its way. For the 1×10^{14} sample, the shape of the He release derivative between 500 and 780°C seen in Figure 9-b, intermediate to the 1×10^{13} and 1×10^{15} cases, suggest two competing release mechanism indeed: a dislocation-driven He escapes from the material preferentially at the lower bound of the temperature range and a second mechanism later discussed for the higher bound.

Peak III is already in the fcc range of Fe and is believed to be due to the release from bubbles, except for the 1×10^{13}, as the vacancy clusters may not be present (or in meagre quantities) due to the lower damage and less He is available to be trapped[39,101]. It is seen that 1×10^{15} has the highest release at this region, indicating that perhaps the most stable vacancy cluster type is around this fluence. A higher fluence value may form a less stable vacancy cluster and more present towards the 800 ºC region, seen by the massive peak for the 1×10^{16}. Some characteristics observed in the diagram agree with the other literature results. Xu and Wirth[102] noticed that, as the fluence increases from 1×10^{14} to 1×10^{15}, the peak I reduces and the III increases, like our results. For them, this was observed both at an implantation energy of 5 keV and 10 keV for both poly-crystal and single-crystal iron.

3.2.2.2. Chromium effect

Similarly, helium desorption experiments were done in Fe-10Cr samples with fluences of 1×10^{14} and 1×10^{16} at/cm^2 (measured fluences of 0.80×10^{14} and 0.572×10^{16} at/cm^2, respectively, similar to that of pure Fe). The results are visible in Figure 9 c) and d). As observed in both cases, chromium delays the helium desorption from 500 °C to 700 °C at 1×10^{14}, and from 700 °C to 850 °C at 1×10^{16}. The phase transition does not seem to provide a sharp He release peak as in pure iron since a significant release peak is not present at around 850 °C for the FeCr specimen with 1×10^{14}.

Most of the He liberated by the 1×10^{16} Fe-10Cr sample is done during a peak starting circa 850 °C, but this is more likely by happenstance given the dissimilarity in peak profile between this peak and that of the $\alpha \rightarrow \gamma$ seen for pure Fe.

Sugano et al. also saw these features of He release from FeCr.[101], as an increased Cr content (5 and 14%) causes a delayed first release peak and less influence from the phase transition. Ono et al.[35] also showed a 20 to 130 °C shift to higher temperatures to most of the peaks of a Fe-10Cr sample. They explained this change using STEM-EELS and showed that Cr segregates around the dislocations and bubbles, diminishing He mobility, and there is also higher nucleation of dislocation loops than in pure iron. The third peak region is present in temperatures above 1100 °C for pure and iron-chromium samples with similar features.

Besides these ramp experiments, three heat treatments with plateaux of constant temperature were done: two for pure iron with a fluence of 1×10^{14} and 1×10^{15} at.cm^{-2}, and one for iron-chromium with a fluence of 1×10^{14}. A model was developed and compared to the experimental data with the results in Figure 10, including the small relative error between them in a). The model is presented and explained in the next section.

3.2.2.3. Helium desorption model

The results displayed in Figure 9 and Figure 10 show the complexity of developing a model with at least three regions of significant peaks and several different processes that may control the gas diffusion. The literature and our theoretical and experimental results can provide some assumptions and considerations to be adopted in the model:

- Based on our results, the He interstitial diffusion calculated by DFT is around 0.06 eV. This value means that He could travel as far as several tens of microns within one second at room temperature[102]. As the He implantation depth in our experiments is centred around 200 nm, all He available prior to annealing is trapped somehow. Conversely, some He should have escaped by interstitial diffusion moments after

implantation, explaining that all determined fluences are below the targeted ones, especially at the higher fluences, as newly implanted He atoms could re-mobilize previously implanted ones.

- It is believed that He could be trapped by various defects such as grain boundaries, impurity-related defects, dislocations, vacancies, helium/vacancy/self-interstitial complexes, and interstitial complexes[35,99,102]. Some are naturally present, such as grain boundaries due to poly-crystals. Others are induced mainly by He irradiation, like vacancies, dislocation and their complexes[89,99].
- Pure iron and iron-chromium sublimate at ultra-low pressures, as in our TDS setup, at temperatures from 950 °C[107–109].
- The vacancy defects recover between 400 and 1000 °C according to[99,110].
- The dislocation defects start to recover from temperatures around 527 °C[89,99].
- Figure 10 shows that all positive T increments seem to "unlock" a new finite quantity of He that exits quickly. On the contrary, no quantitative He is released when the temperature decreases (Figure 10-a ~1000-4000 seconds, Figure 10-c ~1000-2000 and 23000-24000 seconds). Based on our DFT calculations and data gathered in Table 4, the maximum capacity of He of a vacancy reduces as the temperature increase. Thus the He trapping capacity of the whole material should decrease as T increases.

The construction of a model considering all these parameters would require highly complex modelling and computational power work. As a first step, we propose some assumptions based on our DFT calculations to establish a very simplified model:

- The oxidised layer possibly formed at the surface is considered a totally inefficient retention barrier regarding He diffusion.
- The grain boundaries are not considered since the grains are tens of microns in length,

hence considerably more significant than the maximum He implantation depth of 350 nm.

- All the different trapping possibilities for helium are simplified as one type: He is either trapped or not.
- All He concentration at the time t = 0 is trapped.
- Only one-dimensional diffusion is considered (depth).
- When He definitely leaves a trap, it is assumed to diffuse in a defect-free Fe(Cr) crystalline structure. Thus, it quasi-instantaneously escapes the material (Figure 6).
- We considered that once the temperature rises, the vacancy trap capacity decreases, and a fraction of the trapped helium thus leaves the vacancy traps and diffuses quasi-instantaneously towards the surface without being retrapped (since all the vacancy traps are saturated). This phenomenon agrees with the behaviour observed in Figure 10, where the released fraction increases in small steps for each T increment. It means that, for each increment, a new and finite quantity of helium becomes available for detrapping, and only a further increase in temperature could release some additional He. This behaviour could be indirectly confirmed by looking at the few cases in Figure 10a and 10c where T was instead decreased between a plateau T_n and the following T_{n+1}: no or very limited He release was measured for T_{n+1} because the He budget that would have been released for this temperature was already lost at the T_n plateau.

From these considerations, we define the starting parameters for the simplified analytical model:

- C_0: He atoms concentration inside the material before the TDS annealing at time t = 0 (at.m^{-3}).
- C: He atoms concentration inside the material at time t (at.m^{-3}).
- k: rate of helium atoms detrapping (s^{-1}).

- F: fraction available for detrapping.

Then, following Fick's laws, the concentration of helium in the material as a function of time t can be seen in (Eq.7):

$$\frac{\partial C}{\partial t} = -k * C \quad \text{(Eq.7)}$$

The concentration C of helium atoms inside the material and the fractional released gas R evolves with the time t seen in (Eq.8):

$$\begin{aligned} C &= C_0 * (1 + F * (e^{-kt} - 1)) \\ R = 1 - {}^{C}/_{C_0} &= F * (1 - e^{-kt})) \end{aligned} \quad \text{(Eq.8)}$$

These equations can be extended for each temperature step. At given temperature T, the fractional helium released R_i is given by:

$$R_i = F_i * (1 - e^{-k_i t}) \quad \text{(Eq.9)}$$

Where:

- R_i: Fractional released of He for a given temperature T.
- F_i: He fraction available for detrapping at temperature T
- k_i: rate of helium atoms that definitively can escape the trapped state in the material for a given temperature T (s^{-1}).

The function that is fitted in our model corresponds to each fractional released R_i plateau. This fit is done with an iteration loop using a homemade Python code based on the module kmpfit

from the Python Kapteyn library [111]. The adjustment is performed in several steps for each temperature independently, where the end of the plateau n-1 is the beginning of the plateau n. Each parameter is associated with an error value given by the fit procedure and obtained from the standard deviation (F_i_se and k_i_se) and the experimental error bars.

These equations are solved at each temperature plateau in Figure 10, and the F_c and k_c coefficients were found for each one of them. This model represents very well the experimental data, as demonstrated by the "relative" residual in Figure 10. The fitted coefficients F_i and k_i, listed in Supplementary Tables 1-3, do not vary significantly with the temperature within the error bars, corroborating with the DFT calculations, showing that the temperature increase is related to the decrease in the maximum quantity of He that could be accommodated inside the vacancy. This is done in similar steps at each increment of temperature.

This model corroborates well the experimental results with our DFT calculations and surprisingly well fits the experimental TDS data points (Figure 10). However, it is still a simplified approach (notably treating all possible He traps as equivalents). No apparent diffusion coefficient (in m^2/sec) can be deduced from it, although such numerical data is rather eloquent and convenient to gauge the mobility of an atom in a material. In order to obtain an apparent diffusion coefficient, a more complex model should be developed. Several models have been developed considering other possible He pathways or mechanisms. Caturla et al. considered the different substitutional mechanisms for the defect evolution on time [112]. Vassen et al. explored He desorption from iron and Vanadium by considering the bubble-coursing mechanism [113]. Nobel gas desorption models from other materials besides iron may help better understand the diffusion of this kind of gas in general. Poon et al. studied and modelled the deuterium desorption from tungsten based on TDS [114]. Yu et al. used stochastic cluster dynamics to model hydrogen retention in damaged tungsten [115].

4. Conclusions

This article implemented a multiscale approach to understand helium diffusion inside iron better. At the microscopic scale, DFT was used to correctly model the iron unit cell and identify two possible helium insertion sites and their energies: tetrahedral and octahedral. Then, the NEB method was applied to investigate interstitial He migration pathways and their energies. Finally, the transition state theory showed that the octahedral site was not an interstitial site and that only one transition should be significant in He diffusion.

These results were then used in the KMC code to simulate the 3D path of helium in the iron cell. It was identified that in the perfect Fe matrix, diffusion already occurs significantly from low temperatures, and there is no minimal influence of the temperature since the diffusion barrier is 0.06 eV.

Subsequently, the role of chromium and vacancies in helium diffusion was studied. Only a slight difference in the migration energies was observed with the addition of the Cr atom. However, the vacancies were found to play a significant part in the possibility of trapping the helium atom inside it (activation energy of 2.35 eV), thus considerably reducing He mobility. Even a tiny fraction of vacancies can significantly reduce the diffusion coefficient (1 vacancy for 100000 Fe sites would reduce He mobility by six orders of magnitude around 1000 K according to our model). This comes from the vacancy capacity to accommodate many He atoms. One monovacancy can have up to (at least) 9 atoms before a self-interstitial atom (SIA) is created in a high-temperature environment.

The experimental part used two techniques to characterise the helium behaviour in iron alloys further. TEM showed a similar behaviour between helium bubbles in pure iron and iron-chromium alloys, with a high concentration of tiny bubbles of roughly 0.7 nm of radius for the 1×10^{16} He.cm^{-2} samples.

TDS shows that several mechanisms influence helium diffusion. For lower fluences (less than 1×10^{15} He.cm^{-2}), He release is first allowed through dislocations, while helium-vacancy clusters

control it for higher fluences and temperature. A massive He release is also noted along the α → γ crystalline transition.

Based on the DFT calculations, TEM observations and literature data, a simplified (but nonetheless efficient) model for He release from Fe(Cr) is proposed, essentially considering that He escapes the material by the progressively reduced trapping capacity of the traps as T increases. The model's validity is confirmed by the very accurate fit of the helium-released fractions obtained in the TDS plateaux experiments (Figure 10). Combining both theoretical and experimental methods thus helped complement the description and better understand the He desorption mechanisms.

The present study conciliates the high helium diffusion calculated in an iron-perfect cell with its experimental He retention, explained by efficient He accumulation and trapping in vacancies. Possible future research would be studying ways to better cope with this diffusion, including the possibility of adding oxide dispersion nanoparticles in it. In a forthcoming publication, it is envisaged to see the influence of nanoparticles in steels (ODS steels), specially yttria, to cancel He accumulation in ferritic steels.

5. Acknowledgements

One author (V.O.C.) is grateful for funding from the doctoral school PHENIICS (Université Paris-Saclay). We are also thankful to Christophe Diarra and Emmanouil Vamvakopoulos, who helped us manage the calculations cluster: GRIF (http://www.grif.fr). We want to acknowledge Florian Pallier for the help with samples preparation, as well as the technical staff of the JANNuS-Orsay MOSAIC platform at IJCLab, and in particular, Jérôme Bourçois, Silvin Hervé, Philippe Benoit-Lamaitrie and Cédric Baumier. The French RENATECH network partly supported this work for the TEM FIB thin foils preparation by David Troadec at IEMN Lille. Advice and discussions with V.A. Borodin and O. Emelyanova are gratefully acknowledged. This work has been carried out within the framework of the French Federation for Fusion FR-FCM and the Training and Education WP of the EUROfusion

Consortium, funded by the European Union via the Euratom Research and Training Programme (Grant Agreement No 101052200 — EUROfusion). Views and opinions expressed are however those of the author(s) only and do not necessarily reflect those of the European Union or the European Commission. Neither the European Union nor the European Commission can be held responsible for them.

6. References

[1] W. Xiao, X. Zhang, W.T. Geng, G. Lu, Helium bubble nucleation and growth in $\upalpha$-Fe: insights from first–principles simulations, J. Phys.: Condens. Matter. 26 (2014) 255401. https://doi.org/10.1088/0953-8984/26/25/255401.
[2] E.E. Bloom, The challenge of developing structural materials for fusion power systems, Journal of Nuclear Materials. 258–263 (1998) 7–17. https://doi.org/10.1016/S0022-3115(98)00352-3.
[3] N. Gao, M. Victoria, J. Chen, H.V. Swygenhoven, Helium-vacancy cluster in a single bcc iron crystal lattice, J. Phys.: Condens. Matter. 23 (2011) 245403. https://doi.org/10.1088/0953-8984/23/24/245403.
[4] J. Rothaut, H. Schroeder, H. Ullmaier, The growth of helium bubbles in stainless steel at high temperatures, Philosophical Magazine A. 47 (1983) 781–795. https://doi.org/10.1080/01418618308245265.
[5] X. Gai, T. Lazauskas, R. Smith, S.D. Kenny, Helium bubbles in bcc Fe and their interactions with irradiation, Journal of Nuclear Materials. 462 (2015) 382–390. https://doi.org/10.1016/j.jnucmat.2014.10.027.
[6] S.-H. Li, J.-T. Li, W.-Z. Han, Radiation-Induced Helium Bubbles in Metals, Materials (Basel). 12 (2019). https://doi.org/10.3390/ma12071036.
[7] L. Zhang, C.-C. Fu, E. Hayward, G.-H. Lu, Properties of He clustering in α-Fe grain boundaries, Journal of Nuclear Materials. 459 (2015) 247–258. https://doi.org/10.1016/j.jnucmat.2015.01.008.
[8] R. Li, P. Zhang, C. Zhang, X. Huang, J. Zhao, Vacancy trapping mechanism for multiple helium in monovacancy and small void of vanadium solid, Journal of Nuclear Materials. 440 (2013) 557–561. https://doi.org/10.1016/j.jnucmat.2013.03.068.
[9] R. Li, W. Li, C. Zhang, P. Zhang, H. Fan, D. Liu, L. Vitos, J. Zhao, He–vacancy interaction and multiple He trapping in small void of silicon carbide, Journal of Nuclear Materials. 457 (2015) 36–41. https://doi.org/10.1016/j.jnucmat.2014.10.062.
[10] S.J. Zinkle, G.S. Was, Materials challenges in nuclear energy, Acta Materialia. 61 (2013) 735–758. https://doi.org/10.1016/j.actamat.2012.11.004.
[11] P.J. Maziasz, Overview of microstructural evolution in neutron-irradiated austenitic stainless steels, Journal of Nuclear Materials. 205 (1993) 118–145. https://doi.org/10.1016/0022-3115(93)90077-C.
[12] Integrity of Reactor Pressure Vessels in Nuclear Power Plants: Assessment of Irradiation Embrittlement Effects in Reactor Pressure Vessel Steels, INTERNATIONAL ATOMIC ENERGY AGENCY, Vienna, 2009. https://www.iaea.org/publications/7915/integrity-of-reactor-pressure-vessels-in-nuclear-power-plants-assessment-of-irradiation-embrittlement-effects-in-reactor-pressure-vessel-steels.
[13] T. Ishizaki, Q. Xu, T. Yoshiie, S. Nagata, T. Troev, The effect of hydrogen and helium on microvoid formation in iron and nickel, Journal of Nuclear Materials. 307–311 (2002) 961–965. https://doi.org/10.1016/S0022-3115(02)01279-5.

[14] Y. Katoh, M. Ando, A. Kohyama, Radiation and helium effects on microstructures, nano-indentation properties and deformation behavior in ferrous alloys, Journal of Nuclear Materials. 323 (2003) 251–262. https://doi.org/10.1016/j.jnucmat.2003.08.007.
[15] D. Stewart, Y. Osetskiy, R. Stoller, Atomistic studies of formation and diffusion of helium clusters and bubbles in BCC iron, Journal of Nuclear Materials. 417 (2011) 1110–1114. https://doi.org/10.1016/j.jnucmat.2010.12.217.
[16] A. Caro, J. Hetherly, A. Stukowski, M. Caro, E. Martinez, S. Srivilliputhur, L. Zepeda-Ruiz, M. Nastasi, Properties of Helium bubbles in Fe and FeCr alloys, Journal of Nuclear Materials. 418 (2011) 261–268. https://doi.org/10.1016/j.jnucmat.2011.07.010.
[17] Y.-L. Liu, Y. Yu, Z.-H. Dai, Statistical model and first-principles simulation on concentration of HenV cluster and He bubble formation in α-Fe and W, Journal of Nuclear Materials. 456 (2015) 162–173. https://doi.org/10.1016/j.jnucmat.2014.09.059.
[18] J. Ding, P. Zhang, D. Sun, Y. Wang, S. Huang, J. Zhao, Energetics of helium-vacancy complexes in Fe-9Cr alloys from first-principles calculations, Journal of Nuclear Materials. 513 (2019) 143–151. https://doi.org/10.1016/j.jnucmat.2018.10.031.
[19] R.E. Stoller, The influence of helium on microstructural evolution: Implications for DT fusion reactors, Journal of Nuclear Materials. 174 (1990) 289–310. https://doi.org/10.1016/0022-3115(90)90242-F.
[20] H. Ullmaier, The influence of helium on the bulk properties of fusion reactor structural materials, Nucl. Fusion. 24 (1984) 1039–1083. https://doi.org/10.1088/0029-5515/24/8/009.
[21] A.-A.F. Tavassoli, E. Diegele, R. Lindau, N. Luzginova, H. Tanigawa, Current status and recent research achievements in ferritic/martensitic steels, Journal of Nuclear Materials. 455 (2014) 269–276. https://doi.org/10.1016/j.jnucmat.2014.06.017.
[22] Q. Huang, N. Baluc, Y. Dai, S. Jitsukawa, A. Kimura, J. Konys, R.J. Kurtz, R. Lindau, T. Muroga, G.R. Odette, B. Raj, R.E. Stoller, L. Tan, H. Tanigawa, A.-A.F. Tavassoli, T. Yamamoto, F. Wan, Y. Wu, Recent progress of R&D activities on reduced activation ferritic/martensitic steels, Journal of Nuclear Materials. 442 (2013) S2–S8. https://doi.org/10.1016/j.jnucmat.2012.12.039.
[23] A. Kohyama, A. Hishinuma, D.S. Gelles, R.L. Klueh, W. Dietz, K. Ehrlich, Low-activation ferritic and martensitic steels for fusion application, Journal of Nuclear Materials. 233–237 (1996) 138–147. https://doi.org/10.1016/S0022-3115(96)00327-3.
[24] J. Yu, Q. Huang, F. Wan, Research and development on the China low activation martensitic steel (CLAM), Journal of Nuclear Materials. 367–370 (2007) 97–101. https://doi.org/10.1016/j.jnucmat.2007.03.236.
[25] C.-C. Fu, F. Willaime, Interaction between helium and self-defects in α-iron from first principles, Journal of Nuclear Materials. 367–370 (2007) 244–250. https://doi.org/10.1016/j.jnucmat.2007.03.002.
[26] T. Seletskaia, Y. Osetsky, R.E. Stoller, G.M. Stocks, Magnetic Interactions Influence the Properties of Helium Defects in Iron, Phys. Rev. Lett. 94 (2005) 046403. https://doi.org/10.1103/PhysRevLett.94.046403.
[27] C.-C. Fu, F. Willaime, P. Ordejón, Stability and Mobility of Mono- and Di-Interstitials in $\ensuremath{\alpha}$-Fe, Phys. Rev. Lett. 92 (2004) 175503. https://doi.org/10.1103/PhysRevLett.92.175503.
[28] X.T. Zu, L. Yang, F. Gao, S.M. Peng, H.L. Heinisch, X.G. Long, R.J. Kurtz, Properties of helium defects in bcc and fcc metals investigated with density functional theory, Phys. Rev. B. 80 (2009) 054104. https://doi.org/10.1103/PhysRevB.80.054104.
[29] R. Li, P. Zhang, X. Li, J. Ding, Y. Wang, J. Zhao, L. Vitos, Effects of Cr and W additions on the stability and migration of He in bcc Fe: A first-principles study, Computational Materials Science. 123 (2016) 85–92. https://doi.org/10.1016/j.commatsci.2016.06.019.

[30] P. Olsson, C. Domain, J. Wallenius, Ab initio study of Cr interactions with point defects in bcc Fe, Phys. Rev. B. 75 (2007) 014110. https://doi.org/10.1103/PhysRevB.75.014110.
[31] T. Seletskaia, Yu.N. Osetsky, R.E. Stoller, G.M. Stocks, Calculation of helium defect clustering properties in iron using a multi-scale approach, Journal of Nuclear Materials. 351 (2006) 109–118. https://doi.org/10.1016/j.jnucmat.2006.02.016.
[32] F.A. Kröger, H.J. Vink, Relations between the Concentrations of Imperfections in Crystalline Solids, in: F. Seitz, D. Turnbull (Eds.), Solid State Physics, Academic Press, 1956: pp. 307–435. https://doi.org/10.1016/S0081-1947(08)60135-6.
[33] P. Zhang, C. Zhang, R. Li, J. Zhao, He-induced vacancy formation in bcc Fe solid from first-principles simulation, Journal of Nuclear Materials. 444 (2014) 147–152. https://doi.org/10.1016/j.jnucmat.2013.09.048.
[34] K. Ono, K. Arakawa, K. Hojou, Formation and migration of helium bubbles in Fe and Fe–9Cr ferritic alloy, Journal of Nuclear Materials. 307–311 (2002) 1507–1512. https://doi.org/10.1016/S0022-3115(02)01268-0.
[35] K. Ono, K. Arakawa, H. Shibasaki, H. Kurata, I. Nakamichi, N. Yoshida, Release of helium from irradiation damage in Fe–9Cr ferritic alloy, Journal of Nuclear Materials. 329–333 (2004) 933–937. https://doi.org/10.1016/j.jnucmat.2004.04.061.
[36] R. Sugano, K. Morishita, A. Kimura, H. Iwakiri, N. Yoshida, Microstructural evolution in Fe and Fe–Cr model alloys after He+ ion irradiations, Journal of Nuclear Materials. 329–333 (2004) 942–946. https://doi.org/10.1016/j.jnucmat.2004.04.059.
[37] D. Xu, T. Bus, S.C. Glade, B.D. Wirth, Thermal helium desorption spectrometry of helium-implanted iron, Journal of Nuclear Materials. 367–370 (2007) 483–488. https://doi.org/10.1016/j.jnucmat.2007.03.112.
[38] K.Y. Yu, Y. Liu, C. Sun, H. Wang, L. Shao, E.G. Fu, X. Zhang, Radiation damage in helium ion irradiated nanocrystalline Fe, Journal of Nuclear Materials. 425 (2012) 140–146. https://doi.org/10.1016/j.jnucmat.2011.10.052.
[39] H. Lefaix-Jeuland, S. Miro, F. Legendre, Helium Behaviour in Fe-Base Materials: Thermal Desorption and Nuclear Reaction Analyses, Defect and Diffusion Forum. 323–325 (2012) 221–226. https://doi.org/10.4028/www.scientific.net/DDF.323-325.221.
[40] T. Zhu, X.Z. Cao, S.X. Jin, J.P. Wu, Y.H. Gong, E.Y. Lu, B.Y. Wang, R.S. Yu, L. Wei, Helium retention and thermal desorption from defects in Fe9Cr binary alloys, Journal of Nuclear Materials. 466 (2015) 522–525. https://doi.org/10.1016/j.jnucmat.2015.08.044.
[41] P. Hohenberg, W. Kohn, Inhomogeneous Electron Gas, Phys. Rev. 136 (1964) B864–B871. https://doi.org/10.1103/PhysRev.136.B864.
[42] G. Kresse, J. Furthmüller, Efficient iterative schemes for ab initio total-energy calculations using a plane-wave basis set, Phys. Rev. B. 54 (1996) 11169–11186. https://doi.org/10.1103/PhysRevB.54.11169.
[43] G. Kresse, J. Hafner, Ab initio molecular dynamics for liquid metals, Phys. Rev. B. 47 (1993) 558–561. https://doi.org/10.1103/PhysRevB.47.558.
[44] G. Kresse, D. Joubert, From ultrasoft pseudopotentials to the projector augmented-wave method, Phys. Rev. B. 59 (1999) 1758–1775. https://doi.org/10.1103/PhysRevB.59.1758.
[45] P.E. Blöchl, Projector augmented-wave method, Phys. Rev. B. 50 (1994) 17953–17979. https://doi.org/10.1103/PhysRevB.50.17953.
[46] W. Kohn, L.J. Sham, Self-Consistent Equations Including Exchange and Correlation Effects, Phys. Rev. 140 (1965) A1133–A1138. https://doi.org/10.1103/PhysRev.140.A1133.
[47] J.P. Perdew, K. Burke, M. Ernzerhof, Generalized Gradient Approximation Made Simple, Phys. Rev. Lett. 77 (1996) 3865–3868. https://doi.org/10.1103/PhysRevLett.77.3865.
[48] J.P. Perdew, J.A. Chevary, S.H. Vosko, K.A. Jackson, M.R. Pederson, D.J. Singh, C. Fiolhais, Atoms, molecules, solids, and surfaces: Applications of the generalized gradient

approximation for exchange and correlation, Phys. Rev. B. 46 (1992) 6671–6687. https://doi.org/10.1103/PhysRevB.46.6671.
[49] H.J. Monkhorst, J.D. Pack, Special points for Brillouin-zone integrations, Phys. Rev. B. 13 (1976) 5188–5192. https://doi.org/10.1103/PhysRevB.13.5188.
[50] H. J?nsson, G. Mills, K.W. Jacobsen, Nudged elastic band method for finding minimum energy paths of transitions, in: Classical and Quantum Dynamics in Condensed Phase Simulations, WORLD SCIENTIFIC, 1998: pp. 385–404. https://doi.org/10.1142/9789812839664_0016.
[51] L.R. Pratt, A statistical method for identifying transition states in high dimensional problems, J. Chem. Phys. 85 (1986) 5045–5048. https://doi.org/10.1063/1.451695.
[52] R. Elber, M. Karplus, A method for determining reaction paths in large molecules: Application to myoglobin, Chemical Physics Letters. 139 (1987) 375–380. https://doi.org/10.1016/0009-2614(87)80576-6.
[53] G. Henkelman, B.P. Uberuaga, H. Jónsson, A climbing image nudged elastic band method for finding saddle points and minimum energy paths, J. Chem. Phys. 113 (2000) 9901–9904. https://doi.org/10.1063/1.1329672.
[54] A.F. Voter, Classically exact overlayer dynamics: Diffusion of rhodium clusters on Rh(100), Phys. Rev. B. 34 (1986) 6819–6829. https://doi.org/10.1103/PhysRevB.34.6819.
[55] G.H. Vineyard, Frequency factors and isotope effects in solid state rate processes, Journal of Physics and Chemistry of Solids. 3 (1957) 121–127. https://doi.org/10.1016/0022-3697(57)90059-8.
[56] C. Wert, C. Zener, Interstitial Atomic Diffusion Coefficients, Phys. Rev. 76 (1949) 1169–1175. https://doi.org/10.1103/PhysRev.76.1169.
[57] H. Eyring, The Activated Complex in Chemical Reactions, J. Chem. Phys. 3 (1935) 107–115. https://doi.org/10.1063/1.1749604.
[58] E. Wigner, Calculation of the Rate of Elementary Association Reactions, J. Chem. Phys. 5 (1937) 720–725. https://doi.org/10.1063/1.1750107.
[59] F. Bassal, J. Roques, M. Corre, F. Brunet, R. Ketcham, S. Schwartz, L. Tassan-Got, C. Gautheron, Role of Defects and Radiation Damage on He Diffusion in Magnetite: Implication for (U-Th)/He Thermochronology, Minerals. 12 (2022) 590. https://doi.org/10.3390/min12050590.
[60] F. Bassal, J. Roques, C. Gautheron, Neon diffusion in goethite, α-FeO(OH): a theoretical multi-scale study, Phys Chem Minerals. 47 (2020) 14. https://doi.org/10.1007/s00269-020-01083-w.
[61] H. Balout, J. Roques, C. Gautheron, L. Tassan-Got, D. Mbongo-Djimbi, Helium diffusion in pure hematite (α-Fe2O3) for thermochronometric applications: A theoretical multi-scale study, Computational and Theoretical Chemistry. 1099 (2017) 21–28. https://doi.org/10.1016/j.comptc.2016.11.001.
[62] H. Balout, J. Roques, C. Gautheron, L. Tassan-Got, Computational investigation of interstitial neon diffusion in pure hematite, Computational Materials Science. 128 (2017) 67–74. https://doi.org/10.1016/j.commatsci.2016.10.005.
[63] A.B. Bortz, M.H. Kalos, J.L. Lebowitz, A new algorithm for Monte Carlo simulation of Ising spin systems, Journal of Computational Physics. 17 (1975) 10–18. https://doi.org/10.1016/0021-9991(75)90060-1.
[64] D.T. Gillespie, A general method for numerically simulating the stochastic time evolution of coupled chemical reactions, Journal of Computational Physics. 22 (1976) 403–434. https://doi.org/10.1016/0021-9991(76)90041-3.
[65] Y.N. Osetsky, Atomistic Study of Diffusional Mass Transport in Metals, Defect and Diffusion Forum. 188–190 (2001) 71–92. https://doi.org/10.4028/www.scientific.net/DDF.188-190.71.

[66] Y.N. Osetsky, D.J. Bacon, A. Serra, B.N. Singh, S.I. Golubov, One-dimensional atomic transport by clusters of self-interstitial atoms in iron and copper, Philosophical Magazine. 83 (2003) 61–91. https://doi.org/10.1080/0141861021000016793.
[67] D. Mbongo Djimbi, C. Gautheron, J. Roques, L. Tassan-Got, C. Gerin, E. Simoni, Impact of apatite chemical composition on (U-Th)/He thermochronometry: An atomistic point of view, Geochimica et Cosmochimica Acta. 167 (2015) 162–176. https://doi.org/10.1016/j.gca.2015.06.017.
[68] S. Arrhenius, Über die Reaktionsgeschwindigkeit bei der Inversion von Rohrzucker durch Säuren, (1889). https://doi.org/10.1515/zpch-1889-0116.
[69] A. Gentils, C. Cabet, Investigating radiation damage in nuclear energy materials using JANNuS multiple ion beams, Nuclear Instruments and Methods in Physics Research Section B: Beam Interactions with Materials and Atoms. 447 (2019) 107–112. https://doi.org/10.1016/j.nimb.2019.03.039.
[70] IJCLab, JANNuS-SCALP – IJCLab, (n.d.). https://www.ijclab.in2p3.fr/en/platforms/jannus-scalp-en/ (accessed April 12, 2020).
[71] J.F. Ziegler, M.D. Ziegler, J.P. Biersack, SRIM – The stopping and range of ions in matter (2010), Nuclear Instruments and Methods in Physics Research Section B: Beam Interactions with Materials and Atoms. 268 (2010) 1818–1823. https://doi.org/10.1016/j.nimb.2010.02.091.
[72] N. Juslin, K. Nordlund, J. Wallenius, L. Malerba, Simulation of threshold displacement energies in FeCr, Nuclear Instruments and Methods in Physics Research Section B: Beam Interactions with Materials and Atoms. 255 (2007) 75–77. https://doi.org/10.1016/j.nimb.2006.11.046.
[73] S. Jublot-Leclerc, M.-L. Lescoat, F. Fortuna, L. Legras, X. Li, A. Gentils, TEM study of the nucleation of bubbles induced by He implantation in 316L industrial austenitic stainless steel, Journal of Nuclear Materials. 466 (2015) 646–652. https://doi.org/10.1016/j.jnucmat.2015.09.013.
[74] D. Horlait, D. Gosset, A. Jankowiak, V. Motte, N. Lochet, T. Sauvage, E. Gilabert, Experimental determination of intragranular helium diffusion rates in boron carbide (B4C), Journal of Nuclear Materials. 527 (2019) 151834. https://doi.org/10.1016/j.jnucmat.2019.151834.
[75] D. Horlait, R. Faure, B.A. Thomas, N. Devert, M.-L. Amany, G. Carlot, É. Gilabert, A new thermo-desorption laser-heating setup for studying noble gas diffusion and release from materials at high temperatures, Review of Scientific Instruments. 92 (2021) 124102. https://doi.org/10.1063/5.0068858.
[76] J.E. Taylor, The Variation with Wavelength of the Spectral Emissivity of Iron and Molybdenum*, J. Opt. Soc. Am., JOSA. 42 (1952) 33–36. https://doi.org/10.1364/JOSA.42.000033.
[77] T.M. Hartsfield, A.J. Iverson, J.K. Baldwin, Reflectance determination of optical spectral emissivity of metal surfaces at ambient conditions, Journal of Applied Physics. 124 (2018) 105107. https://doi.org/10.1063/1.5042601.
[78] K. Sridharan, T. Allen, M. Anderson, G. Cao, G. Kulcinski, Emissivity of Candidate Materials for VHTR Applicationbs: Role of Oxidation and Surface Modification Treatments, Univ. of Wisconsin, Madison, WI (United States), 2011. https://doi.org/10.2172/1022709.
[79] Y.S. Touloukian, D.P. DeWitt, Thermophysical properties of matter - the TPRC data series. Volume 7. Thermal radiative properties - metallic elements and alloys. (Reannouncement). Data book, Purdue Univ., Lafayette, IN (United States). Thermophysical and Electronic Properties Information Center, 1970. https://www.osti.gov/biblio/5305606 (accessed May 30, 2022).
[80] C.-C. Fu, F. Willaime, Ab initio study of helium in ??-Fe: Dissolution, migration, and clustering with vacancies, Phys. Rev. B. 72 (2005). https://doi.org/10.1103/PhysRevB.72.064117.

[81] D.E. Jiang, E.A. Carter, Diffusion of interstitial hydrogen into and through bcc Fe from first principles, Phys. Rev. B. 70 (2004) 064102. https://doi.org/10.1103/PhysRevB.70.064102.
[82] D. Connétable, M. David, Diffusion of interstitial species (H and O atoms) in fcc systems (Al, Cu, Co, Ni and Pd): Contribution of first and second order transition states, Journal of Alloys and Compounds. 772 (2019) 280–287. https://doi.org/10.1016/j.jallcom.2018.09.042.
[83] R.B. McLellan, Thermodynamics of hydrogen in iron, Scripta Metallurgica. 18 (1984) 1017–1019. https://doi.org/10.1016/0036-9748(84)90280-1.
[84] S.L. Dudarev, R. Bullough, P.M. Derlet, Effect of the alpha-gamma phase transition on the stability of dislocation loops in bcc iron, Phys Rev Lett. 100 (2008) 135503. https://doi.org/10.1103/PhysRevLett.100.135503.
[85] R.J. Kurtz, G.R. Odette, Chapter 3 - Overview of Reactor Systems and Operational Environments for Structural Materials in Fusion Reactors, in: G.R. Odette, S.J. Zinkle (Eds.), Structural Alloys for Nuclear Energy Applications, Elsevier, Boston, 2019: pp. 51–102. https://doi.org/10.1016/B978-0-12-397046-6.00003-4.
[86] Chromium - Element information, properties and uses | Periodic Table, (n.d.). https://www.rsc.org/periodic-table/element/24/chromium (accessed March 2, 2022).
[87] Iron - Element information, properties and uses | Periodic Table, (n.d.). https://www.rsc.org/periodic-table/element/26/iron (accessed March 2, 2022).
[88] E. Martínez, C.-C. Fu, Cr interactions with He and vacancies in dilute Fe-Cr alloys from first principles, Phys. Rev. B. 84 (2011) 014203. https://doi.org/10.1103/PhysRevB.84.014203.
[89] K. Sato, T. Yoshiie, T. Ishizaki, Q. Xu, Behavior of vacancies near edge dislocations in Ni and $\ensuremath{\alpha}\text{\ensuremath{-}}\mathrm{Fe}$: Positron annihilation experiments and rate theory calculations, Phys. Rev. B. 75 (2007) 094109. https://doi.org/10.1103/PhysRevB.75.094109.
[90] S. Takaki, J. Fuss, H. Kuglers, U. Dedek, H. Schultz, The resistivity recovery of high purity and carbon doped iron following low temperature electron irradiation, Radiation Effects. 79 (1983) 87–122. https://doi.org/10.1080/00337578308207398.
[91] T. Seletskaia, Y. Osetsky, R.E. Stoller, G.M. Stocks, First-principles theory of the energetics of He defects in bcc transition metals, Phys. Rev. B. 78 (2008) 134103. https://doi.org/10.1103/PhysRevB.78.134103.
[92] L. Zhang, Y. Zhang, W.-T. Geng, G.-H. Lu, Towards theoretical connection between tensile strength of a grain boundary and segregated impurity concentration: Helium in iron as an example, EPL. 98 (2012) 17001. https://doi.org/10.1209/0295-5075/98/17001.
[93] H.-B. Zhou, S. Jin, X.-L. Shu, Y. Zhang, G.-H. Lu, F. Liu, Stress tensor: A quantitative indicator of effective volume and stability of helium in metals, EPL. 96 (2011) 66001. https://doi.org/10.1209/0295-5075/96/66001.
[94] C.-C. Fu, F. Willaime, Ab initio study of helium in ??-Fe: Dissolution, migration, and clustering with vacancies, Phys. Rev. B. 72 (2005). https://doi.org/10.1103/PhysRevB.72.064117.
[95] J. Marian, V.V. Bulatov, Stochastic cluster dynamics method for simulations of multispecies irradiation damage accumulation, Journal of Nuclear Materials. 415 (2011) 84–95. https://doi.org/10.1016/j.jnucmat.2011.05.045.
[96] S. Nosé, A unified formulation of the constant temperature molecular dynamics methods, J. Chem. Phys. 81 (1984) 511–519. https://doi.org/10.1063/1.447334.
[97] N. Shuichi, Constant Temperature Molecular Dynamics Methods, Progress of Theoretical Physics Supplement. 103 (1991) 1–46. https://doi.org/10.1143/PTPS.103.1.
[98] J. Henry, L. Vincent, X. Averty, B. Marini, P. Jung, Effect of a high helium content on the flow and fracture properties of a 9Cr martensitic steel, Journal of Nuclear Materials. 367–370 (2007) 411–416. https://doi.org/10.1016/j.jnucmat.2007.03.122.

[99] Y.H. Gong, X.Z. Cao, S.X. Jin, E.Y. Lu, Y.C. Hu, T. Zhu, P. Kuang, Q. Xu, B.Y. Wang, Effect of dislocations on helium retention in deformed pure iron, Journal of Nuclear Materials. 482 (2016) 93–98. https://doi.org/10.1016/j.jnucmat.2016.10.014.
[100] J. Chaumont, F. Lalu, M. Salome, A.-M. Lamoise, H. Bernas, A medium energy facility for variable temperature implantation and analysis, Nuclear Instruments and Methods in Physics Research. 189 (1981) 193–198. https://doi.org/10.1016/0029-554X(81)90145-2.
[101] R. Sugano, K. Morishita, A. Kimura, Helium Accumulation Behavior in Iron Based Model Alloys, Fusion Science and Technology. 44 (2003) 446–449. https://doi.org/10.13182/FST03-A375.
[102] D. Xu, B.D. Wirth, Post-implantation thermal desorption of helium from poly- and single-crystalline iron, Journal of Nuclear Materials. 386–388 (2009) 395–399. https://doi.org/10.1016/j.jnucmat.2008.12.141.
[103] S.S. Pati, L.H. Singh, J.C.M. Ochoa, E.M. Guimarãesa, M.J.A. Sales, J.A.H. Coaquira, A.C. Oliveira, V.K. Garg, Facile approach to suppress γ-Fe2O3 to α-Fe2O3 phase transition beyond 600 °C in Fe3O4 nanoparticles, Mater. Res. Express. 2 (2015) 045003. https://doi.org/10.1088/2053-1591/2/4/045003.
[104] R. Sugano, K. Morishita, H. Iwakiri, N. Yoshida, Effects of dislocation on thermal helium desorption from iron and ferritic steel, Journal of Nuclear Materials. 307–311 (2002) 941–945. https://doi.org/10.1016/S0022-3115(02)01098-X.
[105] Y.X. Wang, Q. Xu, T. Yoshiie, Z.Y. Pan, Effects of edge dislocations on interstitial helium and helium cluster behavior in α-Fe, Journal of Nuclear Materials. 376 (2008) 133–138. https://doi.org/10.1016/j.jnucmat.2008.02.066.
[106] F. Gao, H. Heinisch, R.J. Kurtz, Diffusion of He interstitials in grain boundaries in α-Fe, Journal of Nuclear Materials. 351 (2006) 133–140. https://doi.org/10.1016/j.jnucmat.2006.02.015.
[107] P.D. Desai, Thermodynamic Properties of Iron and Silicon, Journal of Physical and Chemical Reference Data. 15 (1986) 967–983. https://doi.org/10.1063/1.555761.
[108] E.Z. Vintaikin, CHROMIUM VAPOR PRESSURE OVER SOLID CHROMIUM-IRON ALLOYS, Doklady Akad. Nauk S.S.S.R. Vol: 118 (1958). https://www.osti.gov/biblio/4306348-chromium-vapor-pressure-over-solid-chromium-iron-alloys (accessed May 17, 2022).
[109] W. Xiong, M. Selleby, Q. Chen, J. Odqvist, Y. Du, Phase Equilibria and Thermodynamic Properties in the Fe-Cr System, Critical Reviews in Solid State and Materials Sciences. 35 (2010) 125–152. https://doi.org/10.1080/10408431003788472.
[110] T. Ishizaki, Q. Xu, T. Yoshiie, S. Nagata, The Recovery of Gas-Vacancy-Complexes in Fe Irradiated with High Energy H or He Ions, Materials Transactions. 45 (2004) 9–12. https://doi.org/10.2320/matertrans.45.9.
[111] J.P. Terlouw, M.G.R. Vogelaar, Kapteyn Package, version 2.3, Kapteyn Astronomical Institute, Groningen, 2015.
[112] M.J. Caturla, C.J. Ortiz, C.C. Fu, Helium and point defect accumulation: (ii) kinetic modelling, Comptes Rendus Physique. 9 (2008) 401–408. https://doi.org/10.1016/j.crhy.2007.09.004.
[113] R. Vassen, H. Trinkaus, P. Jung, Helium desorption from Fe and V by atomic diffusion and bubble migration, Phys. Rev. B. 44 (1991) 4206–4213. https://doi.org/10.1103/PhysRevB.44.4206.
[114] M. Poon, A.A. Haasz, J.W. Davis, Modelling deuterium release during thermal desorption of D+-irradiated tungsten, Journal of Nuclear Materials. 374 (2008) 390–402. https://doi.org/10.1016/j.jnucmat.2007.09.028.
[115] Q. Yu, M.J. Simmonds, R. Doerner, G.R. Tynan, L. Yang, B.D. Wirth, J. Marian, Understanding hydrogen retention in damaged tungsten using experimentally-guided models of

complex multispecies evolution, Nucl. Fusion. 60 (2020) 096003. https://doi.org/10.1088/1741-4326/ab9b3c.
[116] J. Cai, D. Lu, Bonding Character and Formation Energy of Point Defects of He and Vacancy on (001) Surface of bcc Iron by First Principle Calculations, Acta Metallurgica Sinica (English Letters). 26 (2013). https://doi.org/10.1007/s40195-011-0504-z.
[117] Y. Yu, B. Xu, H. Chen, Z. Yang, C. Zhang, Solubility and Anisotropic Migration Behaviors of Helium in bcc Iron Under Strain, Acta Metallurgica Sinica (English Letters). 31 (2017) 1–9. https://doi.org/10.1007/s40195-017-0590-7.
[118] Y. Tateyama, T. Ohno, Stability and clusterization of hydrogen-vacancy complexes in $\ensuremath{\alpha}\ensuremath{-}\mathrm{Fe}:$ An ab initio study, Phys. Rev. B. 67 (2003) 174105. https://doi.org/10.1103/PhysRevB.67.174105.
[119] T. Seletskaia, Yu.N. Osetskiy, R.E. Stoller, G.M. Stocks, Development of a Fe–He interatomic potential based on electronic structure calculations, Journal of Nuclear Materials. 367–370 (2007) 355–360. https://doi.org/10.1016/j.jnucmat.2007.03.018.
[120] H. Wen, Y. Wu, J. Liu, Y. Zheng, Ferromagnetic effects on helium-vacancy complex formation in BCC Fe, J. Phys.: Condens. Matter. 31 (2019) 125401. https://doi.org/10.1088/1361-648X/aafd72.
[121] N. Gao, M. Samaras, H. Van Swygenhoven, A new Fe–He pair potential, Journal of Nuclear Materials. 400 (2010) 240–244. https://doi.org/10.1016/j.jnucmat.2010.03.009.
[122] L. De Schepper, D. Segers, L. Dorikens-Vanpraet, M. Dorikens, G. Knuyt, L.M. Stals, P. Moser, Positron annihilation on pure and carbon-doped $\ensuremath{\alpha}$-iron in thermal equilibrium, Phys. Rev. B. 27 (1983) 5257–5269. https://doi.org/10.1103/PhysRevB.27.5257.
[123] H. Ullmaier, ed., Atomic Defects in Metals, Springer-Verlag, Berlin/Heidelberg, 1991. https://doi.org/10.1007/b37800.
[124] K. Morishita, R. Sugano, B.D. Wirth, T. Diaz de la Rubia, Thermal stability of helium–vacancy clusters in iron, Nuclear Instruments and Methods in Physics Research Section B: Beam Interactions with Materials and Atoms. 202 (2003) 76–81. https://doi.org/10.1016/S0168-583X(02)01832-3.
[125] P.A. Redhead, Thermal desorption of gases, Vacuum. 12 (1962) 203–211. https://doi.org/10.1016/0042-207X(62)90978-8.

Tables

Table 1: Comparison of our helium's insertion energies in the tetrahedral and octahedral sites with other theoretical results from the literature.

	Tetrahedral site E_{ins} **(eV)**	**Octahedral site** E_{ins} **(eV)**
Our results (PBE)	4.57	4.77
Other theoretical (PBE)	4.56[116], 4.46[117]	4.76[116], 4.65[117]
Other theoretical (PW91)	4.37[26]	4.60[26]
Other theoretical (GGA)	4.39[27]	4.55[27]

Table 2: Our and literature insertion energies of helium in the tetrahedral sites of a Fe-Cr system based on the distance between the helium and Cr atoms.

	Tetrahedral site in pure Fe (eV)	**Distance Cr-He: Neighbour, nn, and distance to the tetrahedral site (Å)**	**Tetrahedral site** E_{ins} **(eV)**
Our results (PBE)	4.57	1nn (1.71)	4.66
		2nn (2.65)	4.67
		3nn (3.29)	4.60
		4nn (3.84)	4.59
Other theoretical	4.37[26]	1nn (-)	4.67[29]

V. Oliveira Cavalcanti *et al*, JMN 583 (2023) 154511, https://doi.org/10.1016/j.jnucmat.2023.154511

(PW91)

Table 3: Our substitutional helium formation energy E_{sub}^{f} and vacancy formation energy E_{V}^{f} in BCC iron compared to other DFT, empirical potentials and experimental results present in the literature.

	Vacancy formation energy (E_V^f) (eV)	**Substitutional He energy (E_{sub}^f) (eV)**
Our results (PBE)	2.17	4.37
Other theoretical (PW91)	2.14[28], 2.16[33]	4.08[26], 4.34[28]
Other theoretical (PBE)	2.08[17], 2.13[18]	-
Other theoretical (GGA)	2.00[118]	4.22[80]
Other theoretical (empirical potentials)	-	3.75[119], 3.72[120], 4.22[121]
Experimental results	2.00[122], 1.6-2.2[123]	-

V. Oliveira Cavalcanti *et al*, JMN 583 (2023) 154511, https://doi.org/10.1016/j.jnucmat.2023.154511

Table 4: Summary of the different results for the quantity of He atoms that a single vacancy can accumulate.

	Source	Temperature (K)			
		0 (static-DFT)	**300 (MD)**	**500 (MD)**	**800 (MD)**
Maximal quantity of He atoms	Our results	17 (relaxed volume), 20 (frozen volume)	≤15	≤15	≤9
	N. Gao et al. (2011)[3]	-	16	-	-
	P. Zhang et al. (2014)[33]	At least 20 (frozen volume)	-	-	-
	W. Xiao et al. (2014)[1]	8 (frozen volume)	-	-	-
	Y.-L. Liu et al. (2015)[17]	10 (relaxed volume)	-	-	-

Figures caption

Figure 1: SRIM-calculated depth profile for helium implanted ions (appm) and the resulting damage (dpa) in pure iron.

Figure 2: Visualisation of the interstitial sites in iron. a) is the tetrahedral site, and b) is the octahedral site. (I) corresponds to the visualisation of the site among all the other atoms of the supercell. (II) is a focus of the helium atom in the site with the two nearest unit cells. (III) is the He insertion site.

Figure 3: NEB diagrams of the two possible He interstitial transitions in iron. (a) and (b) represent the transition between S1 and S2 sites with three linked images between them. (c) and (d) represent the transition between S1 and S3 sites with five linked images between them. (e) shows all the possible S1-S2 and S1-S3 transitions for a given site.

Figure 4: NEB diagrams of the possible helium transitions in a supercell of 127 Fe atoms and 1 Cr atom based on the distance to the Cr atom. Our PBE NEB results versus Martínez and Fu GGA drag method results[88].

Figure 5: NEB diagram of the transition from a vacancy to the third nearest tetrahedral site.

Figure 6: Plot of the logarithm of the diffusion coefficient versus the temperature inverse for the different fractions of vacancies. The coefficients were calculated between 300 and 1200 K using a homemade C++ code based on an aleatory vacancy distribution.

Figure 7: View of the He atoms in the vacancy after relaxation of the cell and the comparison with the original iron atoms position without He. The original Fe atoms and bonds are pink, representing

their original positions when no helium atom is added. (I) are the results for frozen volume relaxations, and (II) are for the relaxed volume of the cell.

Figure 8: Transmission Electron Microscopy bright-field images of (I) and (II) for Fe and (III) and (IV) for Fe10Cr samples after He ion implantation at room temperature with a fluence of 1×10^{16} He^{+}/cm^{2}. These images were taken with an underfocus, and an overfocus of -1 and +1 µm, respectively. Some examples of nanometric visible helium bubbles (seen in white) are marked with red arrows. (a) and (b) are the statistical distribution of the bubbles as observed and manually counted on images related to (I) and (II) for Fe and (III) and (IV) for Fe10Cr specimens, respectively.

Figure 9: a) Cumulated helium release profiles from the TDS versus the temperature for a heating ramp of 5°C/min and for pure Fe. b) Instantaneous release as a function of the temperature for pure Fe. c) Cumulate helium release profiles of iron and iron-chromium from the TDS versus the temperature for a heating ramp of 5 °C/min. d) Instantaneous release as a function of the temperature. The different peak regions are indicated in the figure.

Figure 10: Cumulated He release plateaux from TDS versus time for the different samples: a) Fe implanted with a fluence of 1×10^{14}, b) Fe implanted with a fluence of 1×10^{15}, c) FeCr implanted with a fluence of 1×10^{15}. The temperature profile evolution is also presented on the right side. In a), the application of the fit models is used as an example, with the relative error between experimental and simulated results shown.

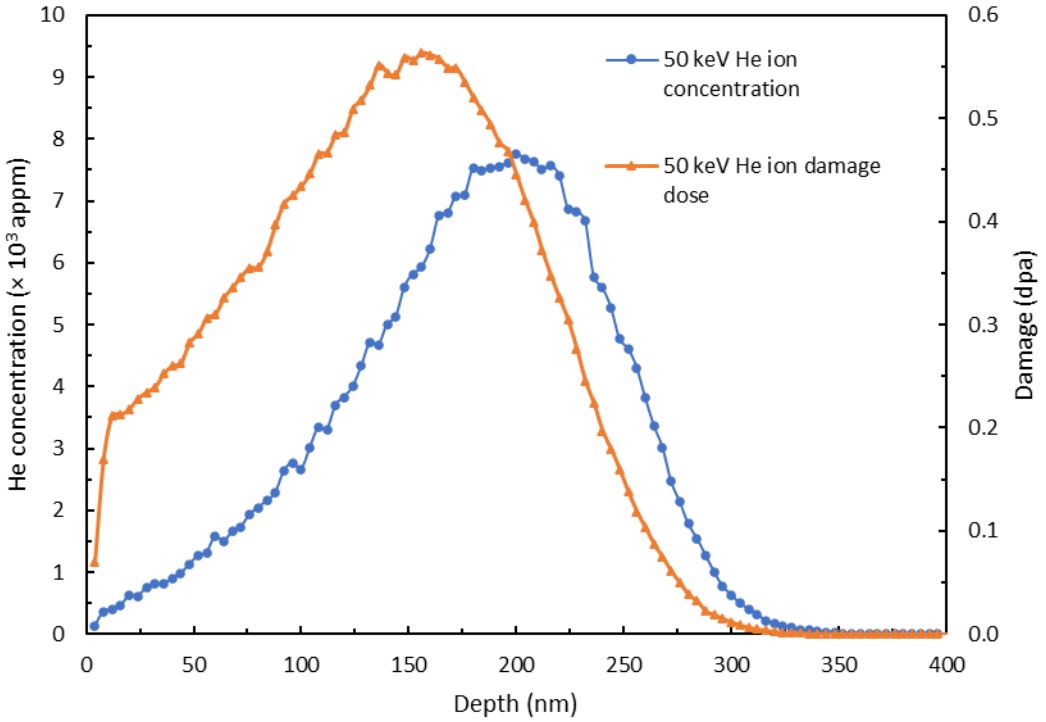

Figure 1

V. Oliveira Cavalcanti *et al*, JMN 583 (2023) 154511, https://doi.org/10.1016/j.jnucmat.2023.154511

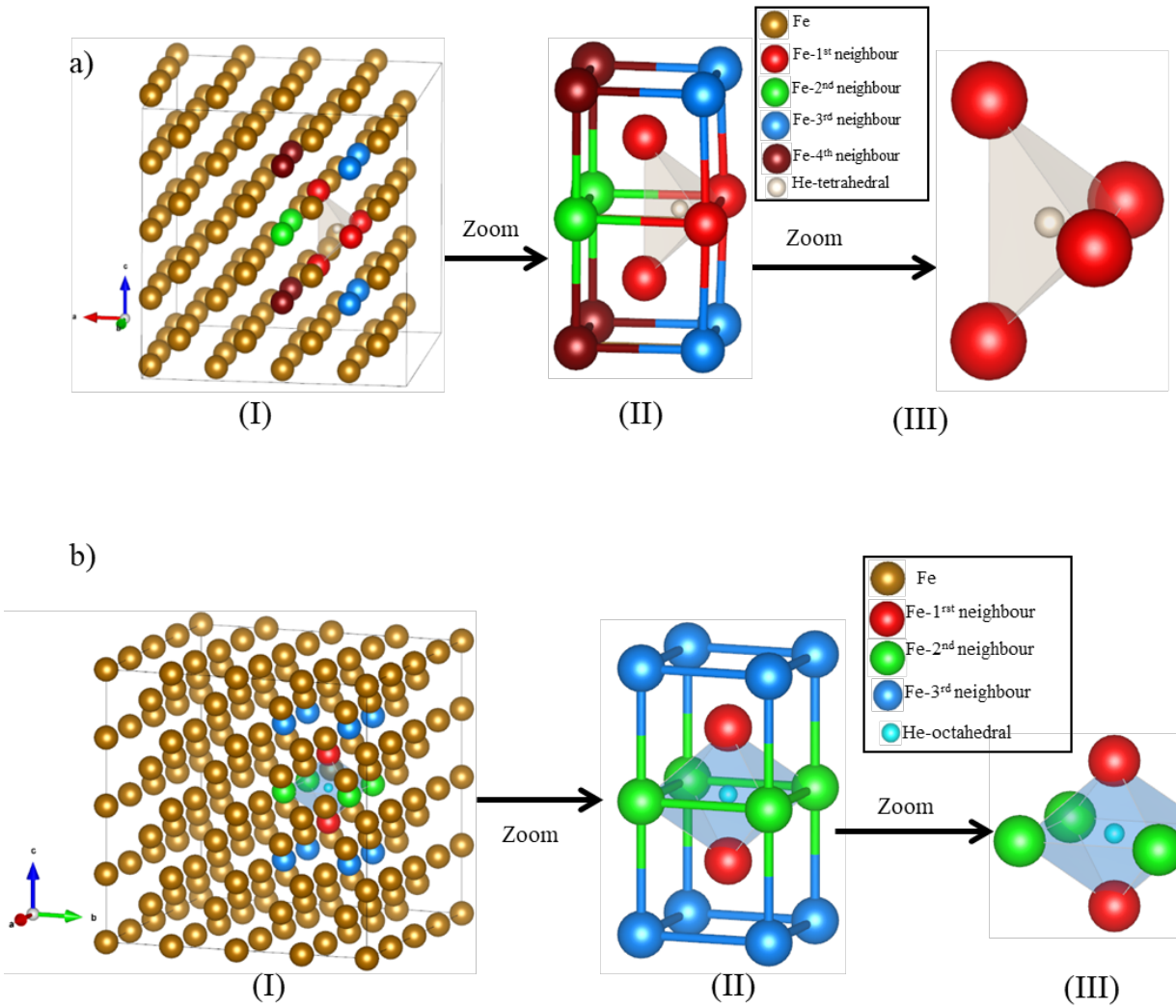

Figure 2

V. Oliveira Cavalcanti *et al*, JMN 583 (2023) 154511, https://doi.org/10.1016/j.jnucmat.2023.154511

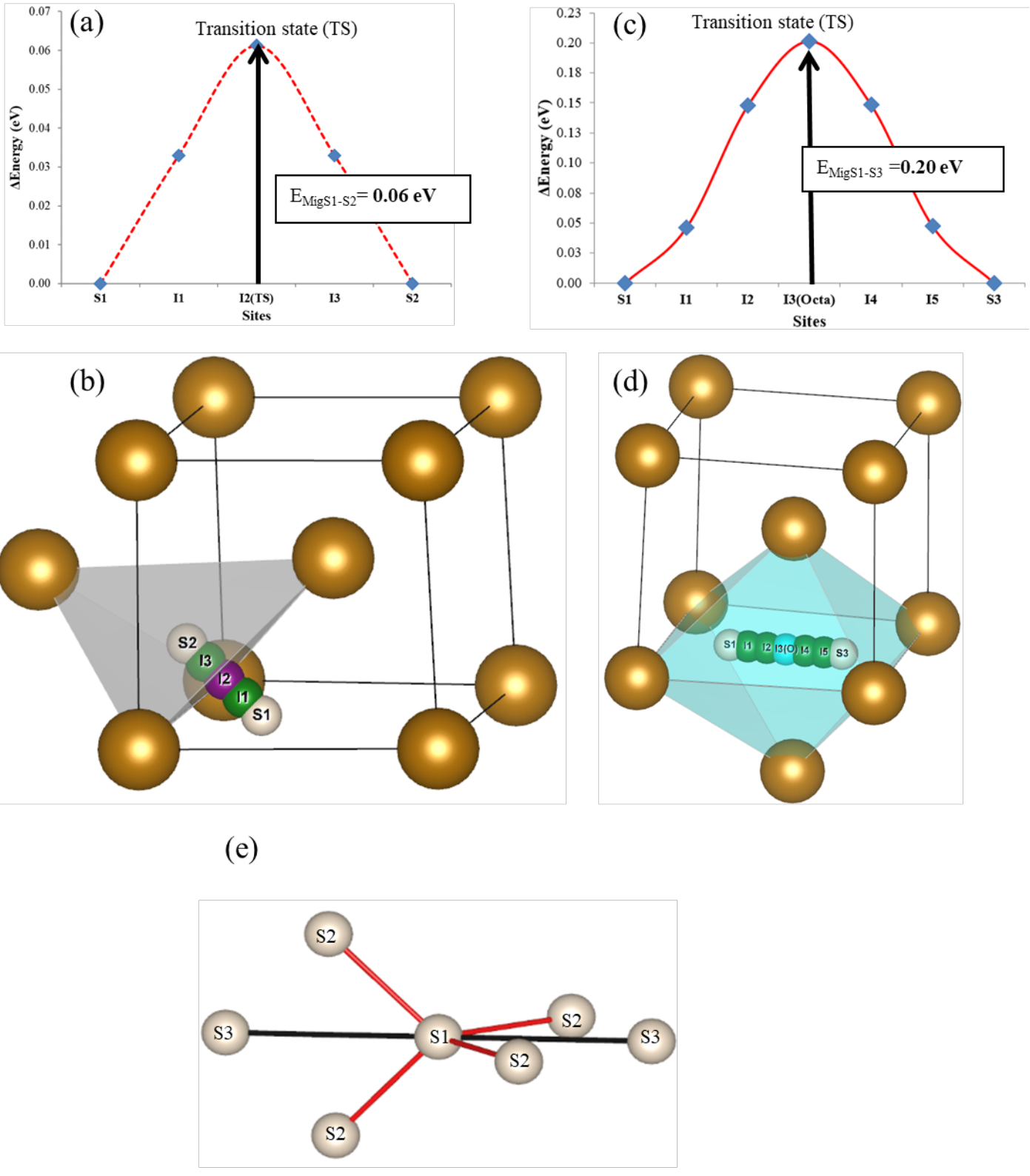

Figure 3

V. Oliveira Cavalcanti *et al*, JMN 583 (2023) 154511, https://doi.org/10.1016/j.jnucmat.2023.154511

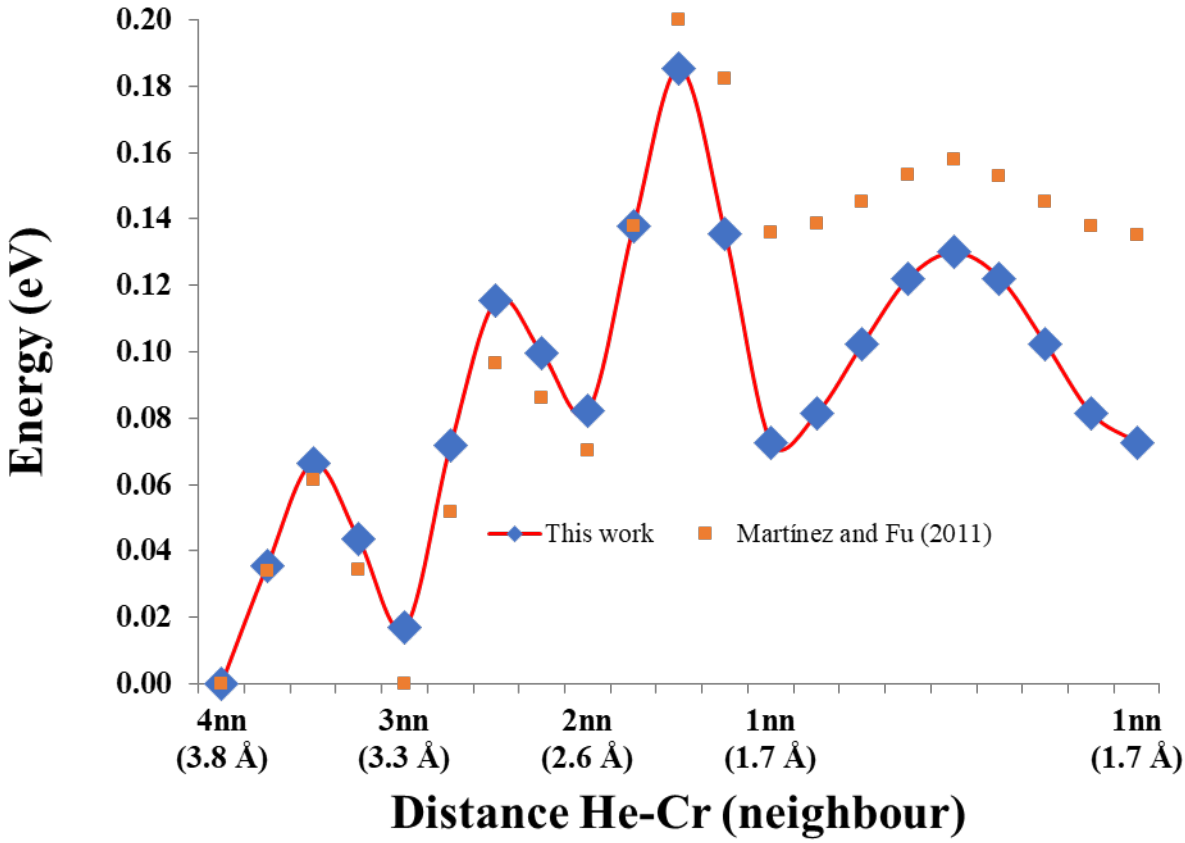
Energy (eV)
0.20
0.18
0.16
0.14
0.12
0.10
0.08
0.06
0.04
0.02
0.00
This work
Martínez and Fu (2011)
4nn
(3.8 Å)
3nn
(3.3 Å)
2nn
(2.6 Å)
1nn
(1.7 Å)
1nn
(1.7 Å)
Distance He-Cr (neighbour)

Figure 4

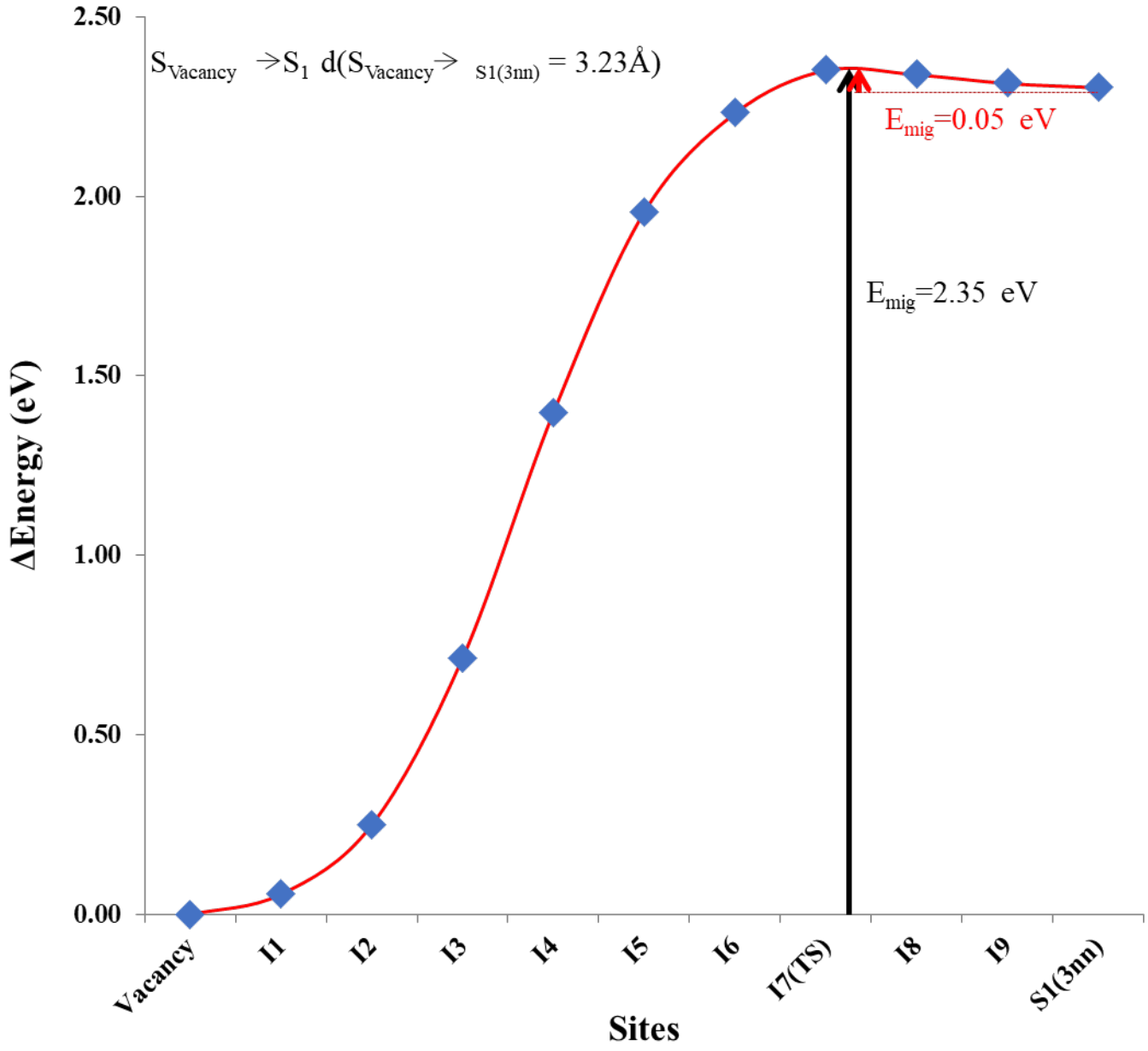
2.50
2.00
1.50
1.00
0.50
0.00
ΔEnergy (eV)
S_Vacancy →S_1 d(S_Vacancy→ S1(3nn) = 3.23Å)
E_mig=0.05 eV
E_mig=2.35 eV
Vacancy
I1
I2
I3
I4
I5
I6
I7(TS)
I8
I9
S1(3nn)
Sites

Figure 5

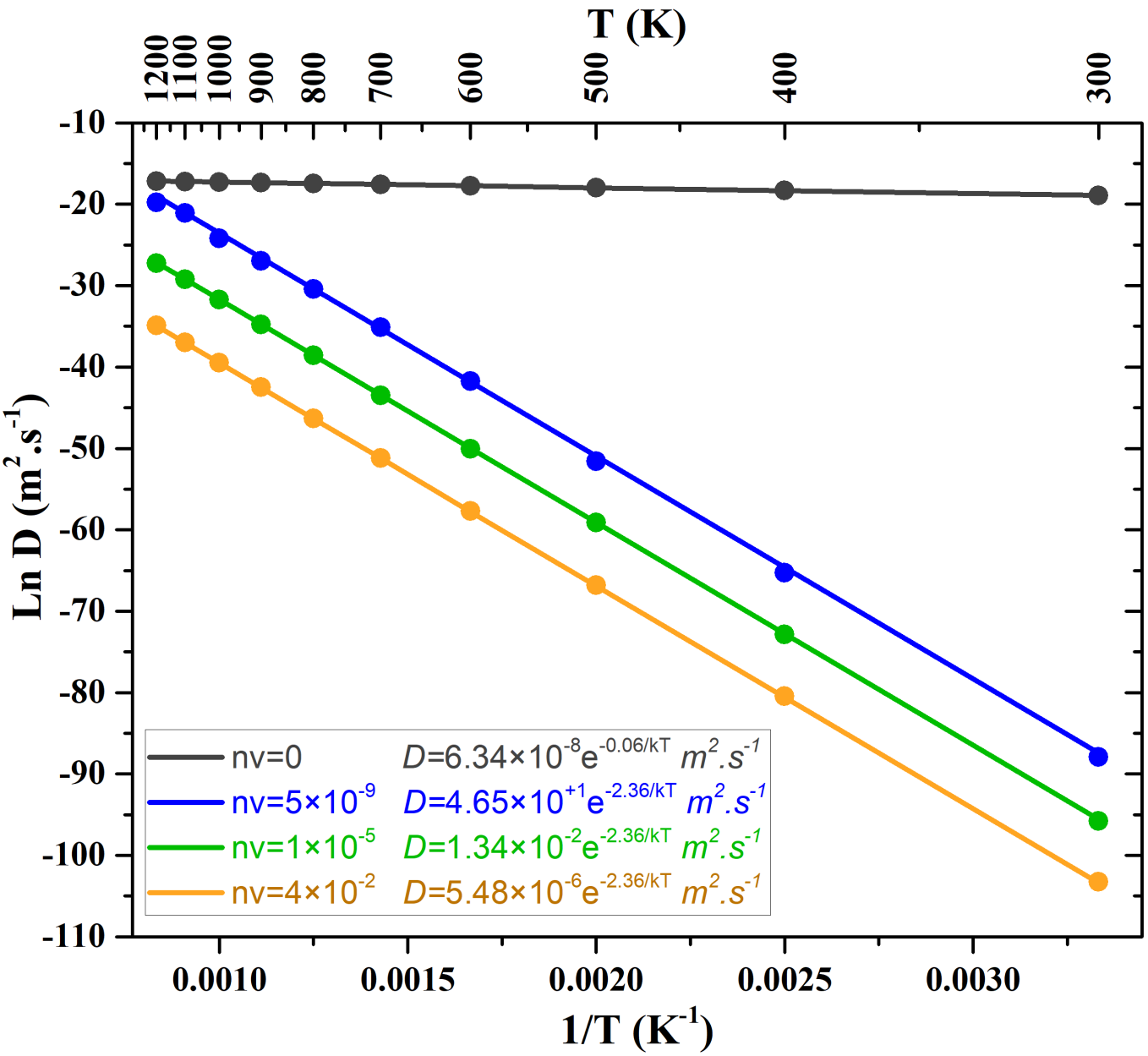

Figure 6

V. Oliveira Cavalcanti *et al*, JMN 583 (2023) 154511, https://doi.org/10.1016/j.jnucmat.2023.154511

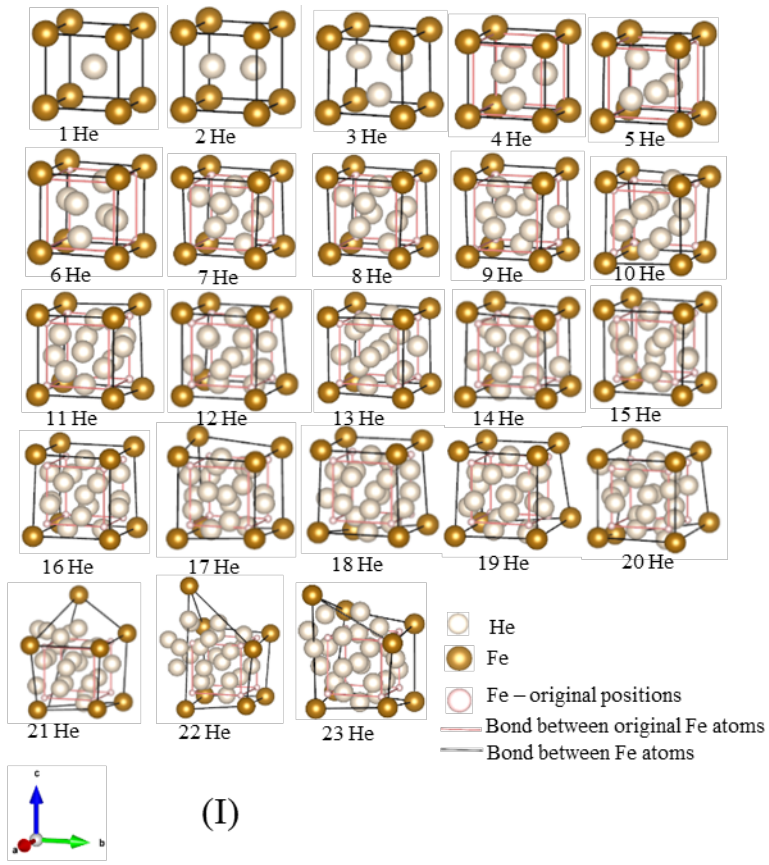

(I)

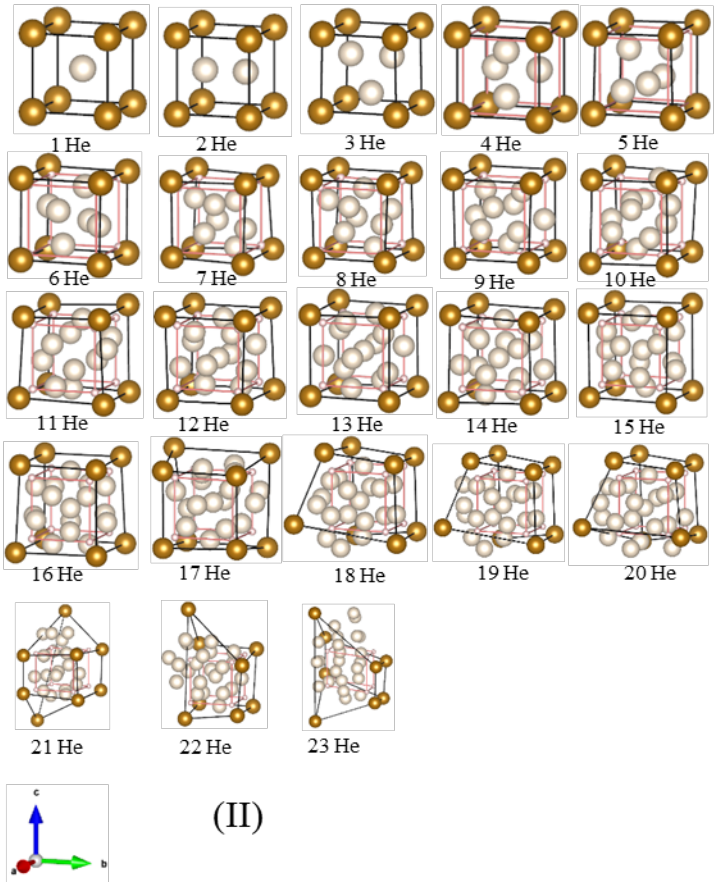

(II)

V. Oliveira Cavalcanti *et al*, JMN 583 (2023) 154511, https://doi.org/10.1016/j.jnucmat.2023.154511

Figure 7

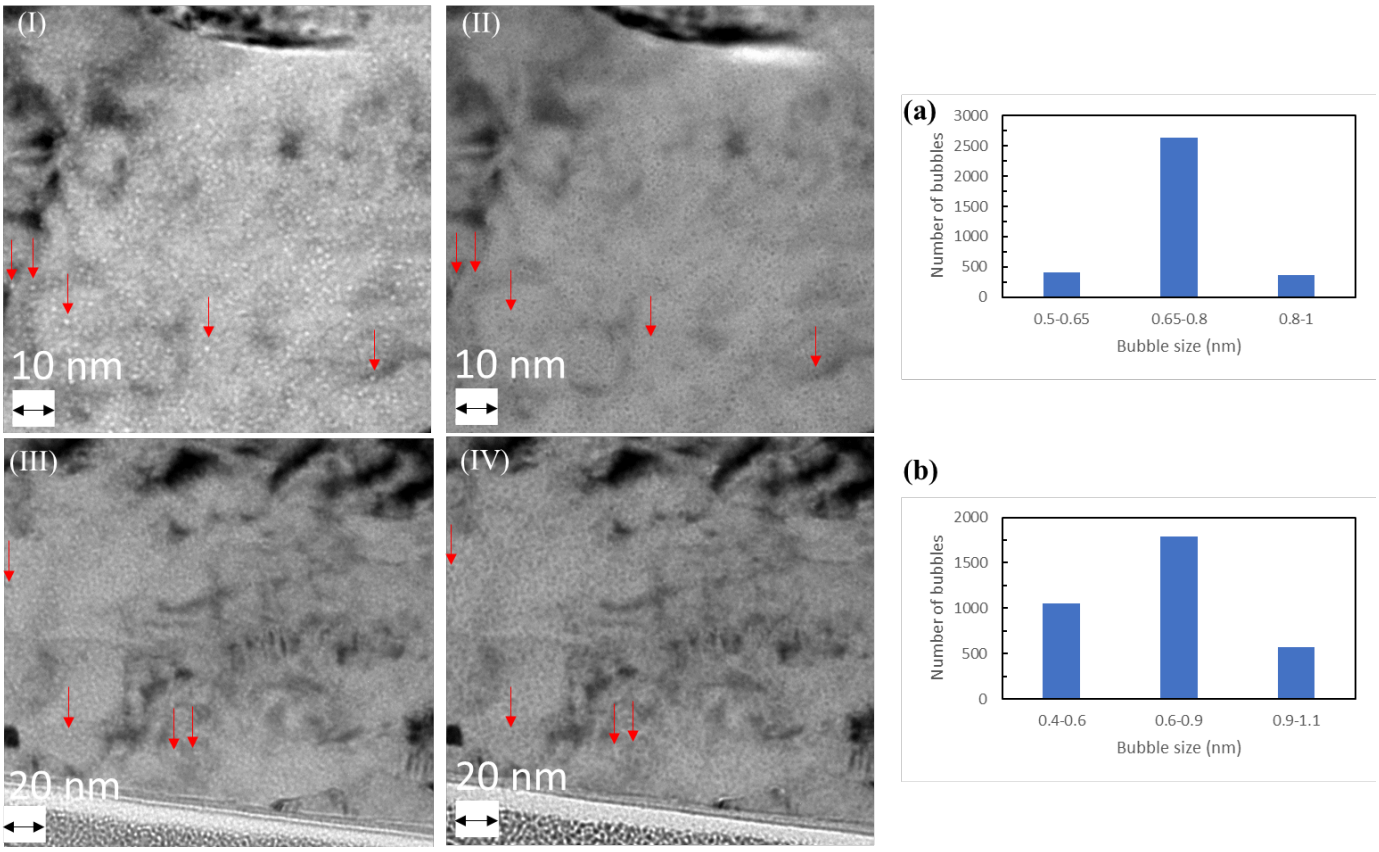

Figure 8

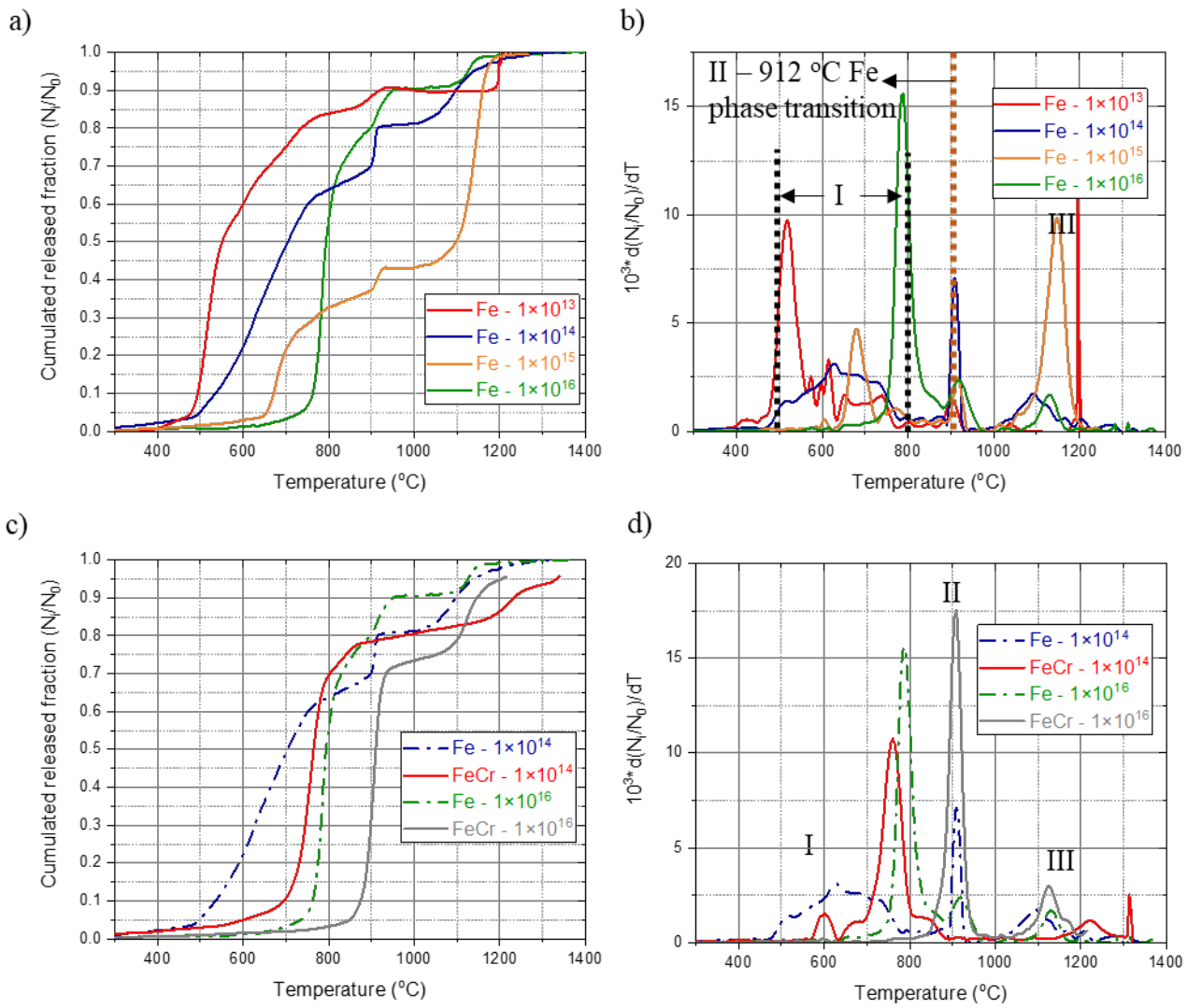
a)
b)
c)
d)
Cumulated released fraction (Nf/N0)
Temperature (°C)
Fe - 1×10^13
Fe - 1×10^14
Fe - 1×10^15
Fe - 1×10^16
II – 912 °C Fe phase transition
I
II
III
10^3* d(Nf/N0)/dT
FeCr - 1×10^14
FeCr - 1×10^16

Figure 9

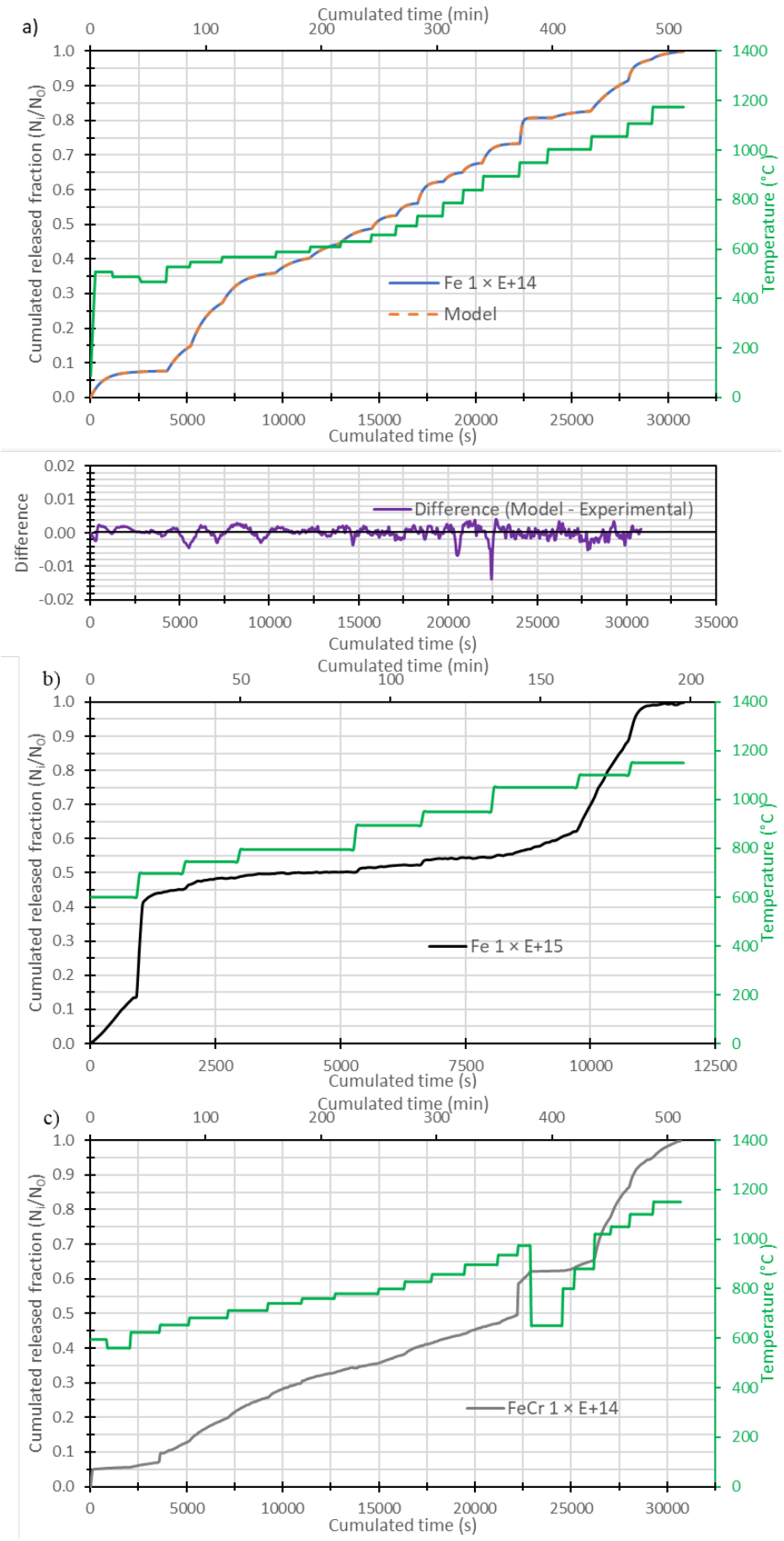

V. Oliveira Cavalcanti *et al*, JMN 583 (2023) 154511, https://doi.org/10.1016/j.jnucmat.2023.154511

Figure 10

Appendix:

Xu and Wirth proposed in their paper [102] to directly relate activation energy associated with He diffusion, considering a first-order dissociation kinetic model. It starts with the following relation : $\frac{dN}{dt} = -Nf\exp\left(-\frac{E}{k_bT}\right)$, where N represents the quantity of He atoms not yet released from a trap, E is the activation energy for the corresponding trap, f is the jumping frequency (the value assumed is 10^{13} Hz[102,104,124]). From this equation, we can derive from the heating rate R, the peak temperature T_p and the activation energy E the following relation: $\ln\left(\frac{R}{T_p^2}\right) = -\frac{E}{k_bT_p} + \ln\left(\frac{fk_b}{E}\right)$. By deriving with the Redhead equation[125], we have a direct relation: $E = \left(\left(\ln\left(\frac{fT_p}{R}\right) - 3.64\right)k_bT_p\right)$. With our value of heating rate of 5 K/s, the activation energy values can be easily derived. For the case used in the present document, for T = 460 ºC corresponds a E value of 2.26 eV. Note this is an approximation, as the dissociation kinetics is not a first-order model, as described by Xu[37], and the model does not consider the interactions between traps with different activation energy values.

b)

Supplementary Table 1: F_i and k_i values as a function of the temperature for the pure iron sample implanted with 1×10^{14} He/cm^2 with the associated standard deviation error bars.

Temperature (°C)	F_i	$F_{i\_}se$	k_i(s^{-1})	$k_{i\_}se$(s^{-1})
506	7.061E-02	2.670E-03	1.839E-03	1.304E-04
486	9.342E-03	1.048E-03	1.080E-03	3.178E-04
466	4.803E-03	4.842E-04	7.126E-04	1.808E-04
526	1.438E-01	6.735E-03	5.717E-04	3.384E-05
546	1.488E-01	2.082E-03	1.022E-03	2.465E-05
566	8.987E-02	1.020E-03	1.114E-03	2.517E-05
587	5.651E-02	8.860E-04	7.217E-04	1.746E-05
608	5.580E-02	1.221E-03	8.573E-04	2.991E-05
629	4.694E-02	8.375E-04	1.259E-03	4.349E-05
656	3.916E-02	8.577E-04	2.129E-03	1.072E-04
692	3.642E-02	6.595E-04	2.864E-03	1.350E-04
732	6.210E-02	6.731E-04	3.201E-03	1.110E-04
785	2.732E-02	1.552E-03	2.610E-03	3.341E-04
837	2.675E-02	9.619E-04	2.919E-03	2.681E-04
893	5.473E-02	7.579E-04	2.599E-03	1.319E-04

948	6.874E-02	5.605E-04	1.293E-02	9.225E-04
1002	2.250E-02	1.079E-03	1.042E-03	1.013E-04
1054	1.961E-01	1.618E-02	3.153E-04	3.245E-05
1106	5.692E-02	9.575E-04	3.069E-03	1.538E-04
1173	2.392E-02	7.466E-04	1.930E-03	1.607E-04

Supplementary Table 2: F_i and $k_i$values as a function of the temperature for the pure iron sample implanted with 1×10^{15} He/cm^2 with the associated standard deviation error bars.

Temperature (ºC)	$\boldsymbol{F_i}$	$\boldsymbol{F_{i\_}se}$	$\boldsymbol{k_i}$**(s^{-1})**	$\boldsymbol{k_{i\_}se}$**(s^{-1})**
697	4.188E-02	8.398E-04	4.873E-03	3.046E-04
745	3.066E-02	6.952E-04	4.099E-03	3.071E-04
795	1.299E-02	3.228E-04	1.792E-03	1.448E-04
894	1.919E-02	7.775E-04	4.279E-03	6.792E-04
950	1.978E-02	4.287E-04	9.012E-03	1.310E-03

Supplementary Table 3: F_i and k_i values as a function of the temperature for the Fe10Cr sample implanted with 1×10^{14} He/cm^2 with the associated standard deviation error bars.

Temperature (°C)	F_i	$F_{i\_}se$	k_i(s^{-1})	$k_{i\_}se$(s^{-1})
594	5.17E-02	2.15E-04	2.41E-02	9.87E-04
560	8.52E-03	3.79E-03	3.29E-04	1.93E-04
623	3.14E-02	3.60E-03	3.94E-04	5.60E-05
653	2.14E-01	2.53E-01	1.11E-04	1.57E-04
682	8.98E-02	2.53E-03	6.32E-04	2.69E-05
711	8.42E-02	1.60E-03	5.78E-04	1.68E-05
740	5.62E-02	1.91E-03	7.53E-04	4.09E-05
760	2.64E-02	1.86E-03	1.89E-03	2.58E-04
779	3.73E-02	3.70E-03	4.97E-04	7.08E-05
799	1.33E-01	3.19E-02	1.63E-04	4.62E-05
828	3.93E-02	1.04E-03	1.14E-03	5.20E-05
857	5.57E-02	3.51E-03	3.78E-04	3.01E-05
896	6.35E-02	6.44E-03	3.73E-04	4.75E-05
935	1.00E-01	5.74E-02	2.65E-04	1.68E-04
880	3.82E-02	1.39E-03	8.24E-04	3.92E-05
1020	2.02E-01	2.52E-02	1.16E-03	1.94E-04

1050	1.36E-01	3.30E-03	1.05E-03	3.61E-05
1100	8.78E-02	1.03E-03	2.28E-03	6.30E-05
1150	6.59E-02	1.36E-03	9.16E-04	3.02E-05